FY20 Lawrence Livermore National Laboratory Experimental Programs at the Omega Laser Facility

R. F. Heeter,[1] F. Albert,[1] S. J. Ali,[1] P. M. Celliers,[1] H. Chen,[1] B.A. Chidester,[2] A. L. Coleman,[1] F. Coppari,[1] T. Döppner,[1] M. Gorman,[1] M. Hohenberger,[1] J. Jeet,[1] A. Lazicki Jenei,[1] S. Jiang,[1] S. F. Khan,[1] Y.-J. Kim,[1] N. Candeias Lemos,[1] M. J. MacDonald,[1] D. Mariscal,[1] E. V. Marley,[1] M. C. Marshall,[1,3] M. J. May,[1] M. Millot,[1] B. B. Pollock,[1] P. L. Poole,[1] D. Rusby,[1] A. M. Saunders,[1] R. Smith,[1] C. Stan,[1] G. F. Swadling,[1] S. Zhao,[4] and A. Zylstra[1]

[1]Lawrence Livermore National Laboratory
[2]University of California, Davis
[3]Laboratory for Laser Energetics, University of Rochester
[4]Lawrence Berkeley National Laboratory

In fiscal year 2020 (FY20), Lawrence Livermore National Laboratory's (LLNL's) High-Energy-Density (HED) Physics and Indirect-Drive Inertial Confinement Fusion (ICF-ID) Programs conducted numerous campaigns on the OMEGA and OMEGA EP Laser Systems. This was the 22nd year of national laboratory collaborative experiments at the Omega Laser Facility since the Nova Laser at LLNL shut down in 1999 (Ref. 1), building upon prior collaborations. In FY20 overall, these LLNL programs led 375 target shots, with 166 shots using only the OMEGA Laser System and 209 shots using only the OMEGA EP Laser System. Approximately 34% of the total number of shots (35 OMEGA shots and 93 OMEGA EP shots) supported the Indirect-Drive Inertial Confinement Fusion Campaign. The remaining 66% (131 OMEGA-only shots and 116 OMEGA EP-only shots) were dedicated to experiments for high-energy-density physics. Highlights of the various HED and ICF-ID campaigns are summarized in the following reports.

In addition to these experiments, LLNL Principal Investigators (PI's) led a variety of Laboratory Basic Science Campaigns using OMEGA and OMEGA EP, including 63 target shots using OMEGA and 49 shots using OMEGA EP. An additional 14 OMEGA EP shots were led by LLNL through a new national fundamental science shot allocation, LaserNetUS.

Overall, LLNL PI's led a total of 501 shots at LLE in FY20. In addition, LLNL PI's supported 71 basic science shots in collaboration with the academic community, including 26 National Laser User's Facility (NLUF) shots, 24 Academic/Industrial Basic Science (AIBS) shots, and 21 LaserNetUS shots led by university collaborators.

Indirect-Drive Inertial Confinement Fusion Experiments

Investigating the Behavior of Diamond Under Shock Compression to Its Melting Line with Pyrometry
Principal Investigator: M. Millot
Co-investigators: Y.-J. Kim and P. M. Celliers

High-density carbon (HDC)—diamond—ablators are used in many ICF designs at the National Ignition Facility (NIF). Understanding the microphysics behavior of this material along the multishock compression path typical for ICF implosions is fundamental. Here we focus on elucidating the behavior of diamond under shock compression to its melting line near 10 Mbar.

The specific goal for this study is to provide more-accurate data than the previous study by Eggert *et al.*[2] more than a decade ago and inform the possibility of lowering the adiabat in HDC implosions on the NIF by tightly benchmarking equation-of-state (EOS) models near the first shock state.

To document the melting temperature of diamond near 10 Mbar, we launched strong unsupported shocks in a planar package containing a diamond plate [Fig. 1(a)]. Using line-imaging Doppler velocimetry (VISAR) and streaked optical pyrometry (SOP), we were able to record high-quality data [Fig. 1(b)] in the 5- to 30-Mbar range. Analysis is ongoing. In addition, using quartz as an impedance-matching standard allowed us to collect high-precision shock pressure–density data along the Hugoniot as described in (Ref. 3).

(a)   (b)

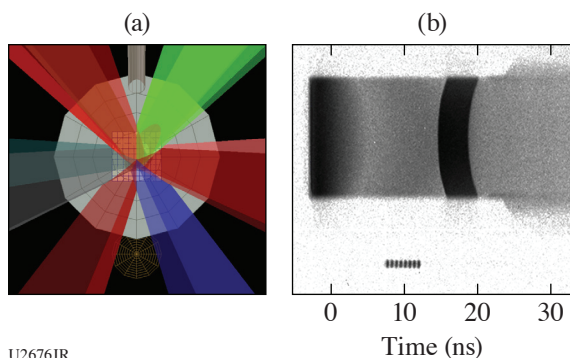0   10   20   30

Time (ns)

U2676JR

Figure 1

(a) VisRad model of the experiment: six beams of the OMEGA laser were used to launch strong shock waves in a diamond sample. (b) Example of a high-quality SOP image exhibiting sharp temporal and spatial resolution.

X-Ray Diffraction of Diamond Under Shock Compression and Shock and Release Near the Melting Line

Principal Investigator: M. Millot
Co-investigators: F. Coppari, D. Braun, A. Jenei, Y.-J. Kim, P. M. Celliers, and J. H. Eggert

Using HDC—diamond—ablators in ICF implosions on the NIF has enabled important advances thanks to its efficiency as an ablator and the possibility of using shorter laser pulses.[4,5] However, the unique thermodynamic properties of carbon present multiple challenges toward reaching higher fusion yield on the NIF. Among these challenges is whether rapid resolidification could occur after the first shock is transmitted to the hydrogen fuel and a release wave propagates backward toward the ablation front. Such a phenomenon would likely be a large source of implosion-quality degradation since the second shock would be launched into a slurry of nano/microcrystalline diamond with a metallic fluid carbon.

Here we focus on elucidating the behavior of diamond under shock compression to completion of the melting line near 12 Mbar [Fig. 2(a)] as well as under shock and subsequent decompression by an impedance-mismatch–generated release wave. The specific goal for this study is to characterize the atomic structure with *in-situ* nanosecond x-ray diffraction.[6]

We launched strong steady shocks in a planar package containing a diamond plate mounted on the powder x-ray diffraction image plate (PXRDIP) diagnostic box [Fig. 2(c)] and collected high-quality x-ray diffraction data [Fig. 2(b)] at unprecedented conditions in the 6- to 15-Mbar range. Ongoing analysis will make it possible to reveal the atomic structure of carbon at those conditions and document the transition from the compressed solid to the metallic warm dense fluid.

Hydrodynamic Response from Nonuniformities in High-Density Carbon

Principal Investigator: S. J. Ali
Co-investigators: P. M. Celliers, R. Briggs, A. Fernandez-Panella, C. Weber, S. W. Haan, and V. A. Smalyuk

Performance and yield from fusion capsules on the NIF are highly dependent on the uniformity of the capsule implosion, and hydrodynamic instabilities are a significant source of performance degradation during the implosion. These instabilities can arise due to, among other reasons, intrinsic heterogeneity within the capsule material. HDC is a polycrystalline diamond material that
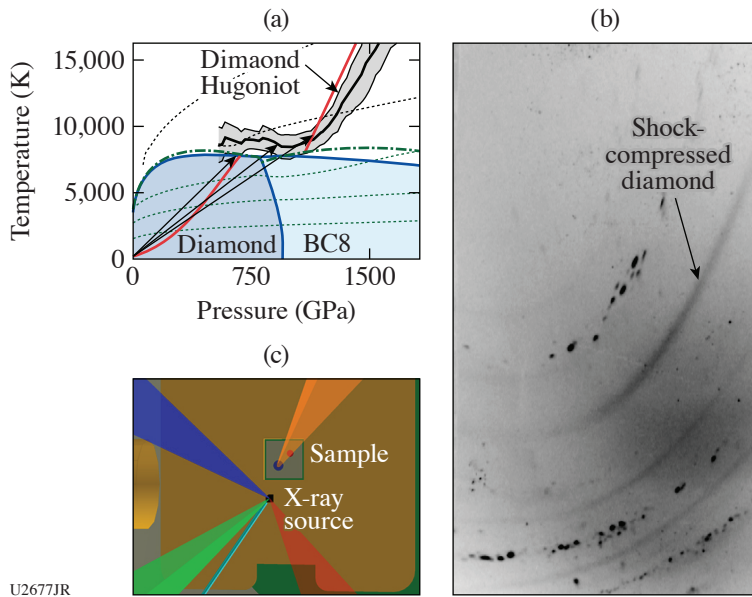
(a)

(b)

(c)

U2677JR

Figure 2
(a) Sketch of our approach to mapping the melting line of diamond near the first shock level. (b) Example of a high-quality x-ray diffraction (XRD) image exhibiting strong lines for shock-compressed diamond. (c) VisRad model of the experiment: one OMEGA EP laser beam was used to launch strong shock waves in a diamond sample, while three additional beams generated a strong x-ray pulse to record an XRD snapshot.

has a complex microstructure, as well as being acoustically anisotropic, which can lead to variations in the shock speed in crystallites of different orientations, potentially seeding instabilities. Additional sources of heterogeneous response include behavior of the grain boundary material, which is often of a different bonding character than the crystallites, voids in the deposited material, and static internal stresses in the polycrystalline structure. The current strategy for reducing the impact of internal heterogeneities is to fully melt the ablator material on the first shock, requiring >12 Mbar for HDC (Refs. 7–9). This strong shock also raises the entropy of the fuel, making it more difficult to reach the high densities required for ignition. As part of the effort to understand both the origin and impact of the velocity nonuniformities in HDC, we have been conducting 2-D velocimetry experiments over the past few years on planar foils under conditions near the first shock in HDC.

While the overarching Capseed Campaign goal is to measure shock-front velocity nonuniformities in ICF ablator materials and quantify the level of nonuniformity, this particular half-day was dedicated to conducting a pressure calibration of our previously measured shock states. While this is a priority for future development, at the moment we cannot simultaneously use line and 2-D velocimetry with the cryogenic D_2 cell. The 2-D velocimetry provides us with significantly more spatial information but measures only the relative velocity, as opposed to the absolute velocity we obtain from line velocimetry measurements. Since the OMEGA laser drive is very consistent, a set of line velocimetry calibration measurements taken at key drive energies used for the previous 2-D velocimetry measurements significantly improves our pressure uncertainties. Results of these line velocimetry measurements with the pressure at breakout are shown in Fig. 3. We covered the range of pressures that were of interest, ~12 Mbar
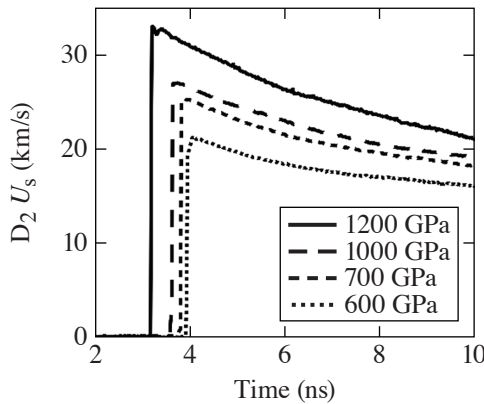

U2678JR

Figure 3
Velocity profiles for the shock velocity in D_2 with estimated HDC stress.

to ~6 Mbar, and by following a more-detailed impedance-matching analysis with uncertainty propagation, we will apply these measurements to constrain the pressure of previously acquired Capseed data.

Investigating Gold Wall/Gas Fill Interactions in an Open Geometry
Principal Investigator: G. F. Swadling
Co-investigators: J. S. Ross, W. A. Farmer, and M. D. Rosen

The AuGasJet Campaign aims to develop a new experimental platform to study the interaction of ablated gold plasma with a He gas fill. The overall purpose of this work is to benchmark simulations and therefore drive progress toward a predictive hohlraum performance model. The experiments use an open geometry that provides excellent diagnostic access to the gold plasma, allowing us to make detailed measurements of the plasma parameters of the gold and helium as they interact using the OMEGA 4ω Thomson-Scattering System. To achieve these goals, the experiments use a supersonic gas nozzle to inject a 0.3-mg/cm^3 plume of gas over the surface of a gold foil (see Fig. 4). The surface of the foil is then heated with the OMEGA 3ω heater beams, and the cloud of plasma that results is probed with Thomson scattering 300 μm from the foil surface. Use of the gas jet removes the need for a "gas bag"; previous experiments using gas bags have shown that the shocks launched by the explosion bag wall significantly perturb the experimental measurements. Using a gas jet also allows us to achieve ICF-relevant gas densities without resorting to a surrogate gas species or a cryogenic target design.

The initial half-day executed in FY20 scoped out the approach and collected some initial data. Four target shots were completed before the gas jet hardware failed. We believe that the hardware failure was due to damage inflicted by the x-ray flux emitted by the gold foil. The design of the gas nozzle has been modified for the follow-up campaign to try to mitigate this failure mode.
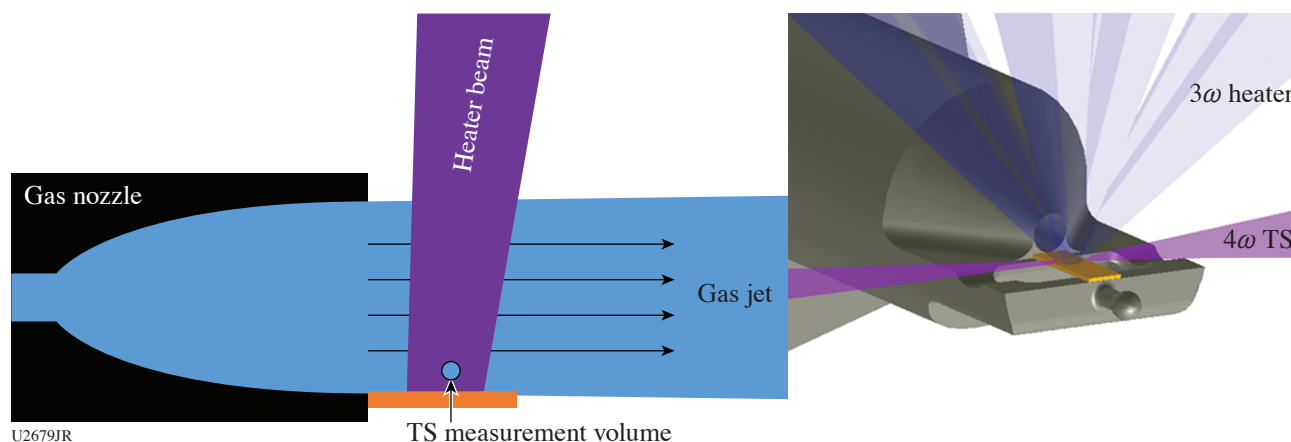

Figure 4
Experimental setup: a gas jet produces a "gas fill" over the surface of a gold foil. TS: Thomson scattering.

Measurements of Biermann-Battery Magnetic Fields Using Three-Particle Backlighting, Plus Au-Ta Foil X-Ray Conversion Study
Principal Investigator: B. B. Pollock (LLNL)
Co-investigators: G. Sutcliffe and C. K. Li (MIT) and J. D. Moody (LLNL)

The MagHohlMultiPBL experiments are attempting to characterize Biermann-battery magnetic-field structures using a new tri-particle backlighter being developed at MIT. The backlighter source is a capsule containing a mixture of DT^{3}He gas, which on implosion produces two populations of protons characteristic of the D–D and D–^{3}He reactions, plus an additional 9.5-MeV deuteron burst from T–^{3}He reactions. The deuteron has different energy and charge-to-mass ratio than either of the proton populations; these three particle groups then each respond differently to electric and magnetic fields. The experimental setup is

shown in Fig. 5, where the capsule is irradiated at the center of the OMEGA target chamber. Two foils, one flat and one curved, are placed 1 cm from the capsule toward ten-inch manipulators (TIM's) containing CR-39 detectors, and the foils themselves are irradiated with one to five beams each. On the surface of each foil, orthogonal density and temperature gradients are produced that give rise to magnetic-field generation through the Biermann-battery mechanism. Protons and deuterons from the backlighter pass tangentially to each foil and are deflected by the fields at the foil surfaces. The CR-39 is in process at MIT, where the three particle signatures are anticipated to reduce degeneracy between electric- and magnetic-field effects and provide information about the field strengths and structures.

In addition to the magnetic-field measurements, several shots were performed on this day to measure x-ray conversion efficiency of AuTa foils of varying composition. This information is being used to inform the choice of material for a new hohlraum design under development on the NIF capable of supporting pre-imposed magnetic fields, as part of a Laboratory-Directed Research and Development Strategic Initiative project. The results in Fig. 6 show that for all conditions tested, the total x-ray flux produced from a five-beam drive on a planar foil varies by only ~5%, which is within the design space tolerance for this new hohlraum material. Based on electrical properties, an alloy with 80% Ta is currently being produced at LLNL for magnetized hohlraum experiments later this year.
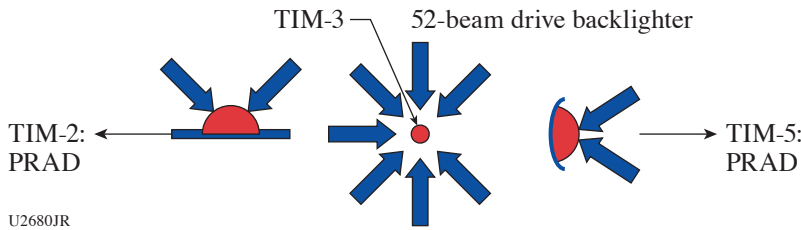

Figure 5
Experimental configuration showing the backlighter capsule at target chamber center (TCC) and both Au foils (each 1 cm from the capsule). The foil toward TIM-5 is actually concave into the page so that protons and deuterons pass tangential to the surface.
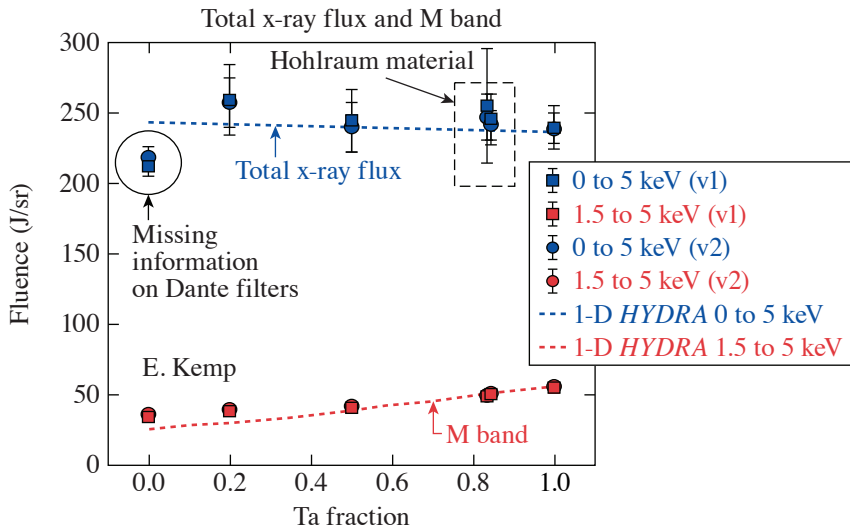

Figure 6
Dante measurements of x-ray flux from a driven foil at varying Au:Ta fractions.

Magnetic-Field Amplification in Imploding Cylindrical Targets
Principal Investigator: B. B. Pollock (LLNL)
Co-investigators: J. R. Davies and J. L. Peebles (LLE) and J. D. Moody (LLNL)

The BFieldAmp Campaign seeks to demonstrate high magnetic-field generation (~kT) by compressing a modest seed field (tens of T) in a converging cylindrical target. The experimental configuration is shown in Fig. 7, where a D_2-filled cylinder sits coaxially within a magneto-inertial fusion electrical discharge system (MIFEDS) coil near the center of the OMEGA target
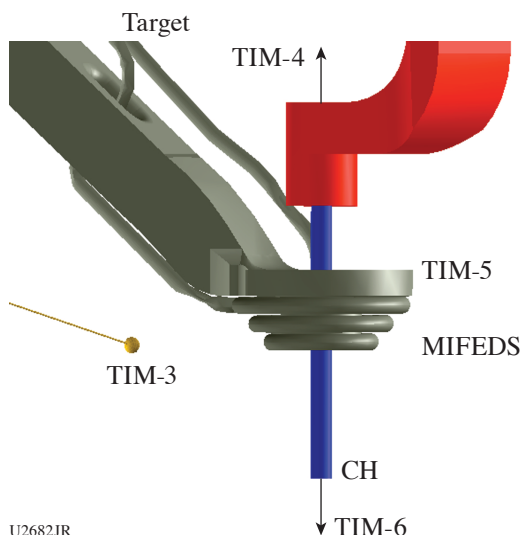
Figure 7
Experimental configuration showing the plastic cylindrical target inside of a MIFEDS coil and the D^{3}He-filled capsule. The target is aligned along the TIM-4–TIM-6 axis, while the primary proton radiography axis is from TIM-3 to TIM-2.

chamber. The MIFEDS produces the seed magnetic field, and at peak field, 40 OMEGA beams uniformly compress a 500-μm-long region of the cylinder, similar to the work of Knauer *et al.*[10] With a modest convergence ratio of 10, the tube is compressed from a 560-μm diameter to a 50- to 60-μm diameter, resulting in an expected ~100× amplification of the magnetic field. The primary measurement of the field is proton radiography, where the protons are supplied by the implosion of a D^{3}He-filled capsule 1 cm from the tube center. Protons are collected on CR-39 detectors 30 cm from the target, and the changes in proton trajectory with and without an applied magnetic field can be determined and then used to infer the magnetic-field strength. Before the CR-39 can be analyzed, it undergoes a chemical-etching process to reveal pits left by the impacts of the arriving protons; that process is still underway for these experiments. Following a successful demonstration of field amplification, this target platform will be used for additional high magnetic-field physics studies, where 1- to 10-kT fields are required but unattainable through conventional pulsed-power schemes.

Shock-Propagation Measurements in Magnetized Quartz Samples with Laser-Driven Magnetic Fields
Principal Investigator: B. B. Pollock (LLNL)
Co-investigators: J. R. Davies and D. N. Polsin (LLE) and J. D. Moody (LLNL)

The BFieldLoopEP Campaign has previously investigated the dynamics of high current and magnetic-field generation in capacitor-coil–style targets.[11,12] The FY20 shot days in this campaign transitioned the focus to observing the effects of these large (hundreds of T) magnetic fields on external systems and developing platforms for using them as seed fields in related physics studies. In particular, these experiments measured shock propagation through quartz samples with and without pre-imposed magnetic fields using the active shock breakout (ASBO) system on OMEGA EP in various shock-drive and magnetic-field–drive configurations.

The experimental configuration is shown in Fig. 8, where the capacitor-coil target is comprised of Au foil folded to produce a half-loop region with a radius of 250 μm. A 0.6- to 1-mm-wide region is removed in the curved section, leaving behind 300-μm-wide strips on each end of the target. One to three long-pulse beams are focused to the front side of the target, which drives a blow-off plasma, sourcing a current through the strips and producing a magnetic field along the loop axis (here aligned with the 4ω probe axis). The magnetic field rises rapidly to ~100 T in the first 1 ns of the 10-ns drive, then more slowly to 300 to 400 T by the end of the drive. An additional long-pulse beam is used to drive the surface of a quartz sample embedded between the Au strips, where the magnetic field is the strongest. This launches a shock into the quartz, propagating perpendicular to the magnetic field. The primary measurement is the shock propagation, recorded by the OMEGA EP ASBO system with a line of sight normal to the rear surface of the quartz, to record the shock breakout time and other features.

Figure 9 shows a calculation of breakout times as a function of applied magnetic-field strength for a variety of shock pressures, as well as the change in breakout between magnetized and unmagnetized propagation conditions. For 5- to 10-mbar shocks
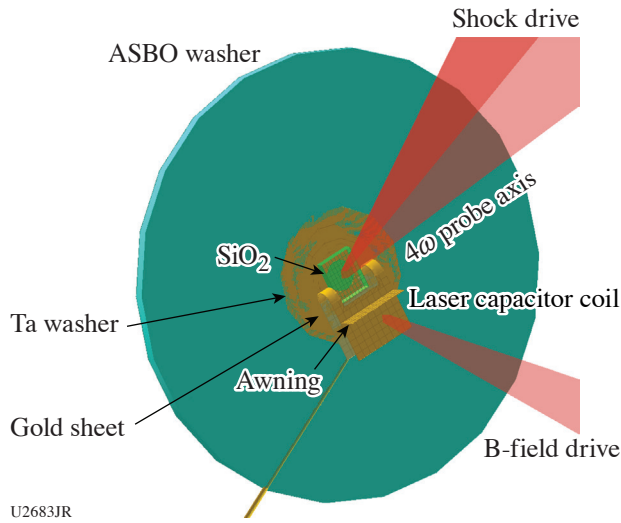
Figure 8
Experimental configuration showing the capacitor-coil target, the quartz sample, and nominal laser pointing for the B field and shock drive beams. The target structure is mounted onto a light-tight Ta washer and backed by a standard ASBO washer.
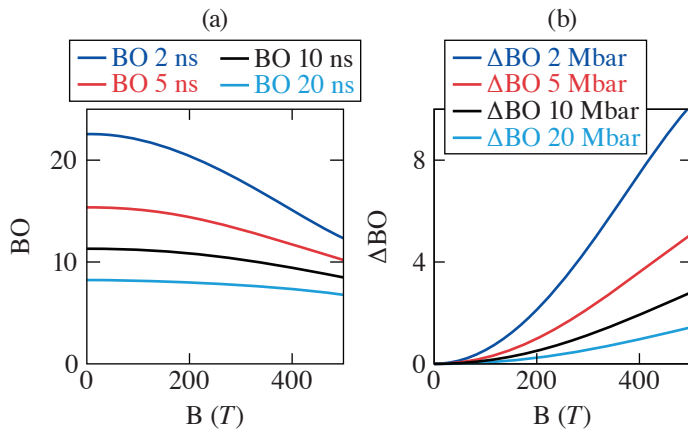

Figure 9
(a) Calculated shock breakout times as a function of shock pressure and applied magnetic field. (b) Change in breakout between magnetized and unmagnetized propagation conditions.

(which is the range probed here), the magnetic field should reduce the breakout time by roughly a few hundred ps for the 100- to 300-T range of applied fields sampled during the shock drive and propagation. Initial analysis of the ASBO data suggests that the magnetic field reduces the breakout time by 100 to 200 ps across the conditions investigated, but further analysis is needed to quantify the uncertainties. Future experiments will increase the temporal sensitivity of the instrument configuration and seek to increase the strength of the applied magnetic field.

Increasing Laser-Accelerated Particle Energies with "Shaped" Short Pulses
Principal Investigator: D. Mariscal (LLNL)
Co-investigators: G. G. Scott and T. Ma (LLNL) and R. Simpson (MIT)

Newer kJ-class short-pulse (ps) lasers such as the NIF's Advanced Radiographic Capability (ARC) laser have recently been shown to be able to accelerate protons to energies that far exceed conventional scalings. While these results are encouraging, the proton energies necessary for probing indirectly driven ICF experiments remain 2× higher than currently achievable with ARC. A new concept, inspired by ARC's capability to deliver multiple short-pulse beams to the same location with specified delays, was tested on OMEGA EP by delivering both short-pulse beams to a single target in order to create pseudo-shaped short laser pulses.

The experimental geometry for these TeBoost shots is shown in Fig. 10. Both short-pulse beams were defocused to $R_{80} \sim$ 45 μm in order to simulate ARC-like laser conditions. One beam delivered 275 J in 4.5 ps, while the trailing beam delivered 275 J in 3 ps. Cu foils, 1-mm diameter by 35 μm thick, were used as targets. The ultrafast x-ray streak camera (UFXRSC) and the time-resolved channel of the high-resolution spectrometer (HRS) monitored the relative timing of the beams on target. Particle diagnostics including radiochromic film (RCF) and the electron positron–proton spectrometer (EPPS) were used to monitor the particle characteristics for each shot. Particle spectra were recorded from single-beam shots before combining the beams and varying their relative timing throughout the day. Overall there were eight shots: four with a single beam and four with combined beams. A preliminary analysis of the data (Fig. 11) indicates that electron temperatures and yields when pulse combinations were used were lower than a single 4-ps beam by itself. Radiochromic film stacks and EPPS proton spectra similarly showed that the maximum proton energy performed worse with dual-beam configurations; however, one shot with dual beams did show a large increase in proton flux. These data suggest that the use of shaped short pulses could increase the efficiency of MeV proton sources driven by NIF's ARC through the use of multibeam configurations.
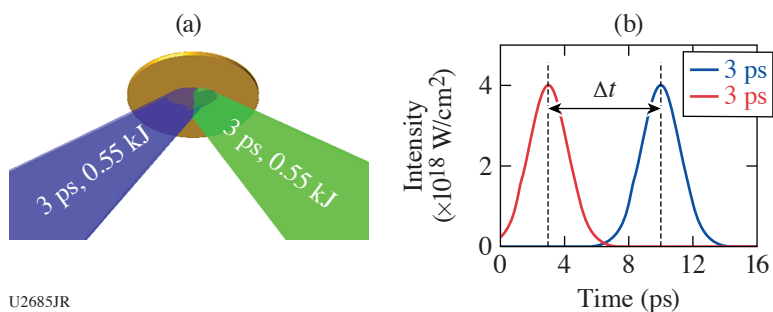

U2685JR

Figure 10
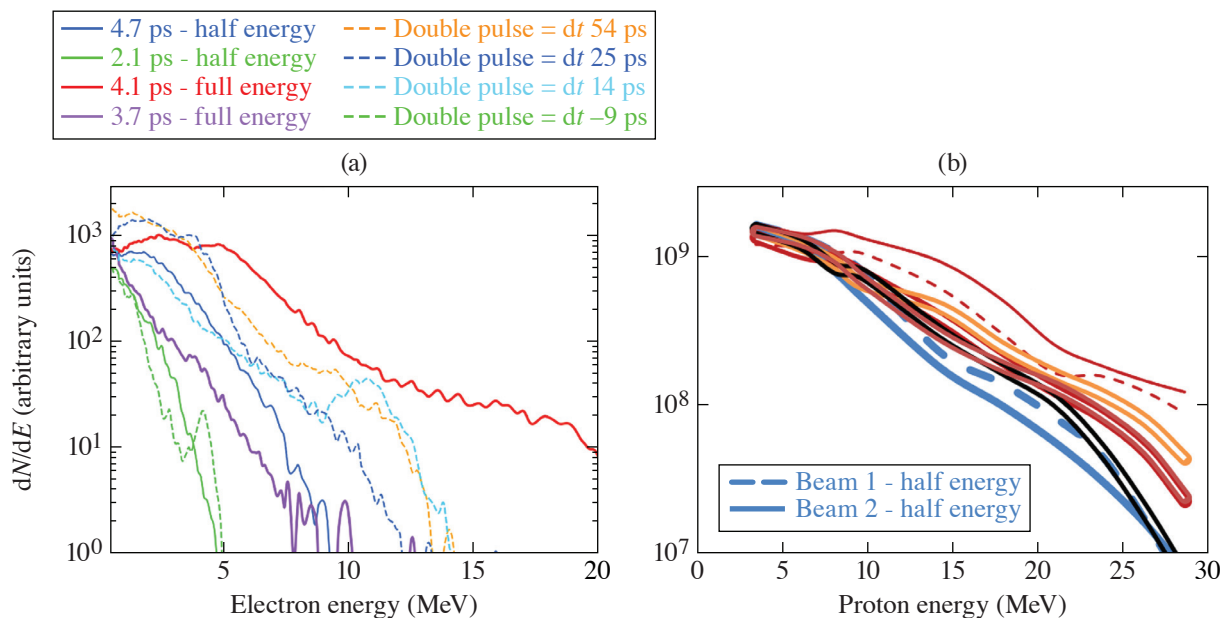(a) Experimental configuration showing the two short-pulse beams incident on the foil target, the location of the diagnostics, and (b) an example of the pulse shapes and definition of Δt for Fig. 11.

U2686JR

Figure 11
(a) Electron and (b) proton spectra from the EPPS spectrometer. The best-performing shot was a single 4-ps beam with 550 J, compared to double pulses with equivalent energy.

Enhanced Yields of Energetic X-Rays, Positrons, and Electrons Using Capillary-Structured Targets

Principal Investigator: N. Lemos

Co-investigators: H. Chen, S. Kerr, D. Rusby, J. Williams, and A. J. Mackinnon

Micron-sized capillaries have the potential to enhance >0.1-MeV x rays, electrons, and positron production.[13] As a short laser pulse (<100 fs) propagates through the capillaries, the ionized electrons are pulled into the laser due to the focusing magnetic and electric field developed at the capillaries' surface. These electrons are then accelerated by direct laser acceleration, and when the laser beam reaches the flat high-Z converter, these electrons acquire significant kinetic energy that can be converted into higher-energy x rays and/or positrons. These targets showed great improvement when using a low-energy (5-J), short-duration (40-fs) laser pulse when compared to a simple flat high-Z converter.[13]

Here, we intend to extend this concept to the longer (10-ps), more-energetic (900-J) laser pulse of OMEGA EP. Four different targets were tested where the period and microwire diameter were varied (Fig. 12). The highly ordered Si microwire arrays were attached to a 1×1-mm gold cylinder that was used to convert electrons into x rays and positrons. Figure 13 shows the measured electron distribution temperature (blue tringles) and yield (red circles) directly looking at the back of the target for the five targets used in this experiment. The flat target (1×1-mm gold cylinder) consistently showed the lowest temperature and yield throughout the experiment. Despite the result shown in Fig. 13, due to the lack of statistics and shot-to-shot variability, it is impossible to identify which microwire produces the highest temperature and yield.

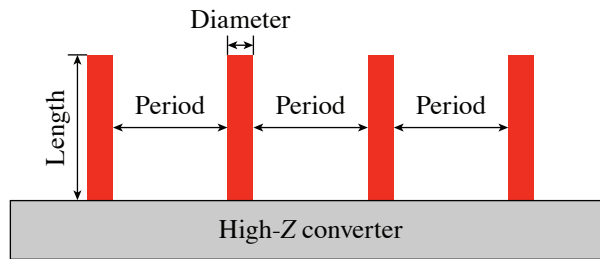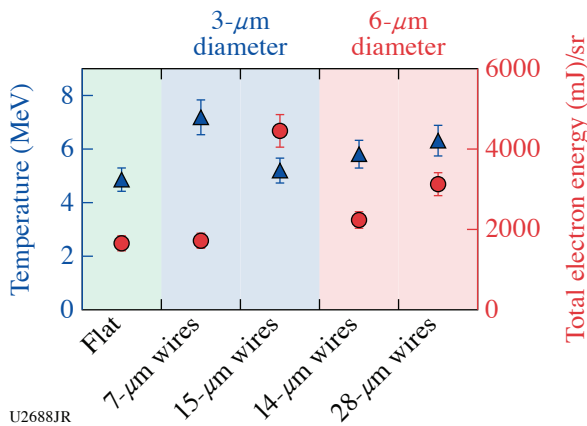| Period	Length	Wire diameter
28 μm	20 to 30 μm	6 μm
14 μm	20 to 30 μm	6 μm
15 μm	20 to 30 μm	3 μm
7 μm	20 to 30 μm	3 μm

U2687JR

Figure 12

Table and figure describing the four microwires used on the experiment.

U2688JR

Figure 13

Electron-beam–distribution temperature and energy for the five targets used in this experiment, organized by the wire diameter and the period spacing between the wires.

To characterize the x-ray source imaging capabilities of these targets, a high-density object [image-quality indicator (IQI)][14] was radiographed. The brightest x-ray image was obtained using a microwire with a 28-mm period. This image had an x-ray signal that was 2× higher than the one obtained with a flat target.

Further analysis is in progress, but these targets show great improvement over flat targets, opening a route to high-energy backlighter capability for HED and ICF.

Broadband MeV X-Ray Source Development Using Compound Parabolic Concentrators Targets
Principal Investigator: N. Lemos (LLNL)
Co-investigators: D. Rusby, J. Williams, A. Pak, and A. J. Mackinnon (LLNL), and W. Theobald (LLE)

Compound parabolic concentrators[15] (CPC's) have been shown to increase laser–solid coupling by further focusing the laser beam and/or increasing the plasma scale length by plasma confinement inside the CPC. Here we study how CPC's can enhance the production of MeV photons and how pre-plasma inside the CPC's affects the performance of a CPC using the OMEGA EP laser.

The OMEGA EP laser with 900 J and a 10-ps pulse duration was focused into a CPC that was coupled to a 2 × 2-mm Ta cylinder used to generate x rays through bremsstrahlung (Fig. 14). Two different CPC's were used with two tip sizes, 25 μm and 50 μm. Figure 15 shows the measured x-ray distribution temperature (blue triangles) and yield (red circles) directly looking at the back of the target for the three targets used in this experiment. The target with a 25-μm tip diameter CPC consistently showed the highest temperature and yield, and the flat target (2 × 2-mm Ta cylinder) consistently showed the lowest yield throughout the experiment. The target with a 50-μm tip diameter CPC showed a lower temperature than the flat target, but a higher yield. This
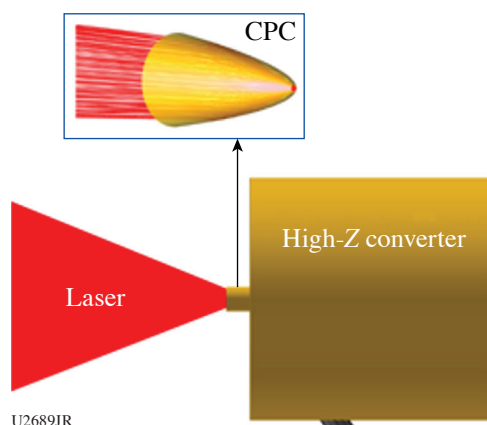

Figure 14
Target configuration used in the experiment; CPC target attached to a 2 × 2-mm Ta cylinder.
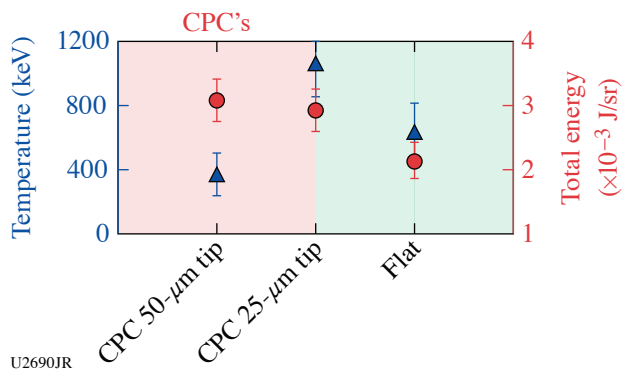

Figure 15
X-ray distribution temperature and energy for the three targets used in this experiment.

is possibly an indication that the CPC is collecting and focusing the energy on the wings of the laser spot (36-μm diameter at $1/e^2$) into the CPC tip (larger than the spot size), increasing coupling. To understand how pre-plasma inside a CPC affects the performance of a CPC, a UV beam with 0.7 J was used to create a pre-plasma inside the CPC. This beam was fired before the main pulse with a controlled time delay from 0.25 ns to 3 ns. To evaluate if the CPC performance was degrading over time, x-ray images of an IQI were taken. Time delays over 0.5 ns showed a reduction of the x-ray signal reaching a maximum of 2× for a delay of 3 ns. Figure 16 shows the shadowgraph of the target before the main pulse hits it when a UV beam with delays of –3 ns, –0.5 ns, and –0.25 ns is used. At –0.25 ns [Fig. 16(c)] there is no apparent external CPC expansion, but from 0.5 ns to 3 ns the external CPC expansion is visible, justifying the reduction on the x-ray signal on the radiographs. Further analysis is in progress, but these targets show a great improvement over flat targets, opening a route to high-energy backlighter capability for HED and ICF.
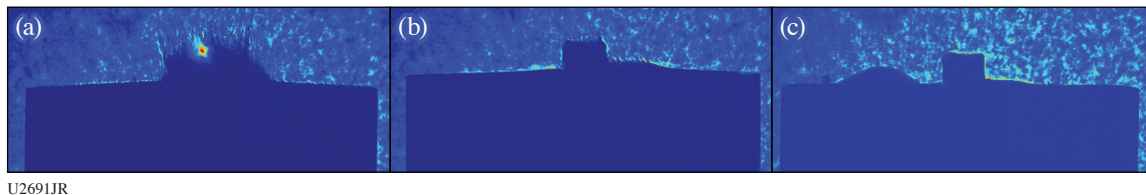

U2691JR

Figure 16
Shadowgraph of the target 100 ps before the main pulse arrives when a UV beam is fired (a) 3 ns, (b) 0.5 ns, and (c) 0.25 ns before the main pulse.

High-Energy-Density Campaigns
1. Material Equation-of-State and Strength Measured Using Diffraction

High-Pressure Chemistry in Shocked TATB
Principal Investigators: M. C. Marshall,[*] M. G. Gorman, A. Fernandez-Pañella, S. M. Clarke, J. H. Eggert, and L. D. Leininger (LLNL); and D. N. Polsin (LLE)
[*]Currently at LLE

TATB (1-3-5-triamino-2,4,6-trinitrobenzene) is a high explosive known for its insensitivity to external stimuli like high temperatures and impacts. When shocked to a sufficiently high pressure, TATB ($C_6H_6N_6O_6$) chemically reacts into solid carbon condensates and gaseous products including N_2, CO, CO_2, and H_2O. In previous OMEGA EP campaigns, we measured the Hugoniot of single-crystal TATB to 83 GPa (Ref. 16) and began searching for the solid carbon reaction products using *in-situ* x-ray diffraction. We found that TATB single crystals remain highly textured (single crystal-like) when shocked to ~50 GPa. At ~50 to ~90 GPa, there was no longer evidence of the compressed single crystals. Instead, a powder diffraction line was detected that was consistent with compressed diamond. The goal of the FY20 campaign is to confirm the diamond product formation at high pressure.

The targets comprised an epoxy or Be ablator, a TATB sample, and a LiF window. In some shots, there was no "ablator" and the TATB was irradiated directly. Two OMEGA EP beams were stacked in time to produce an ~20-ns drive that supported a nearly steady shock through the TATB. The remaining two OMEGA EP beams were incident on an Fe or Cu backlighter foil, generating the x-ray source for the diffraction measurements. Diffraction patterns of the target shortly before the shock exited the TATB were recorded using the PXRDIP diagnostic. VISAR was used to measure interface velocities needed to determine the TATB pressure during the x-ray probe time.

A diffraction line consistent with the (111) reflection of compressed diamond was again observed above 45 GPa (example in Fig. 17) for all shots with an epoxy ablator and one shot using the TATB itself as the ablator. An additional second line consistent with the (220) reflection in diamond was observed in two shots above 100 GPa. Work is ongoing to decouple diffraction from diamond produced in the shocked TATB from possible diamond produced in the reshocked epoxy ablator.
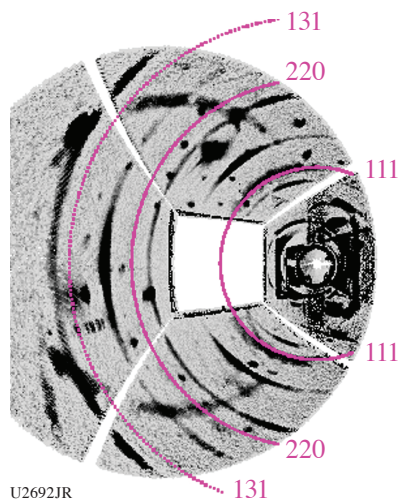
Figure 17
Stereographic projection of diffraction data for shot 31374 showing diffraction consistent with the (111) reflection of compressed diamond. Unlabeled powder diffraction rings are from the W pinhole.

Resolidification Kinetics of Tin Along a Shock Ramp Path
Principal Investigators: M. Gorman and R. Smith

The goal of these experiments was to study the solidification kinetics of shock-melted tin. Tin samples were first shock compressed to 90 GPa to ensure the sample had completely melted. Using the pulse-shaping capability of OMEGA EP, the sample was then ramp compressed to 200 GPa back into the solid phase. The crystal structure of the Sn sample was then investigated using the PXRDIP diagnostic.

Samples consisted of a 130-μm Be ablator with a 1-μm Au preheat shield deposited on it. The ablator was bonded to a 35-μm Al pusher and a 12-μm Sn sample. A 150-μm LiF window was then bonded to the sample.

Our VISAR data show good agreement with our designs from hydrodynamic simulations (Fig. 18). The Sn sample was initially shocked to 90 GPa, where shock melting is known to occur, before it was ramp compressed to 200 GPa. The Ge backlighter was timed to probe the sample at peak pressure, and the collected diffraction data are consistent with the bcc phase (Fig. 19).

Our results clearly show that the bcc phase of Sn can nucleate from the melt on nanosecond time scales and also help to constrain the high-pressure melt curve of Sn. These lattice-level measurements support the equation-of-state effort on the NIF, which has studied Sn along various shock ramp paths.
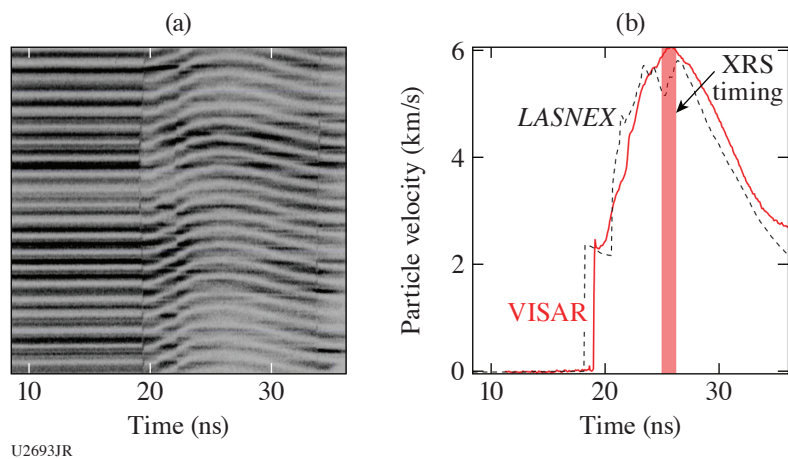

Figure 18
(a) Raw VISAR data and (b) analyzed velocity data of shot 32953 that show Sn shocked to 90 GPa and then ramped to 200 GPa. The analyzed velocity data (red curve) are in very good agreement with the outputs of our hydrodynamic simulations (dashed black curve). The red-shaded bar indicates the timing and duration of the Ge backlighter source.
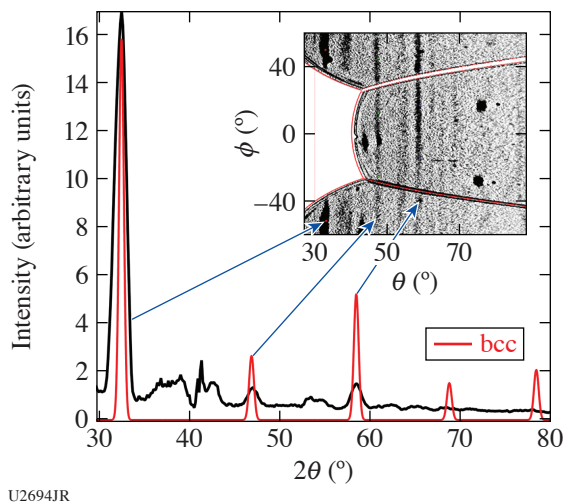
Figure 19
Image-plate diffraction data of shot 32953 with integrated diffraction profile. Several diffraction peaks were observed with at least three found to be consistent with bcc Sn. Other weak diffraction features were found to originate from the Al pusher (not shown).

U2694JR

2. Material Equation-of-State Using Other Techniques

The Metastability Limit of Liquid Water Under Compressive Freezing into Ice VII
Principal Investigators: M. C. Marshall, M. Millot, D. E. Fratanduono, Y.-J. Kim, F. Coppari, P. C. Myint, J. L. Belof, J. H. Eggert, R. F. Smith, and J. M. McNaney (LLNL) and D. M. Sterbentz (University of California, Davis)

Kinetics can play an important role in the transformation of matter to different high-pressure phases over the short time scales associated with dynamic-compression experiments. Many theoretical and experimental works have investigated the effects of kinetics on the rapid freezing of water into the ice VII phase. We are studying the metastability limit of ramp-compressed liquid water undergoing freezing into ice VII at the fastest compression rates to date (~1 GPa/ns).

Experiments were done on the OMEGA EP laser. One laser beam was used to shock the 12%Br-CH reservoir that released across a vacuum gap and isentropically loaded the water cell shown in Fig. 20(a). A thin water layer (~15 μm), created using a diving board configuration inside the water cell, was ramp compressed to ~15 GPa over ~15 ns. Since ice VII is more dense than liquid water, there is a volume collapse in the thin water layer upon freezing. This causes a stress release on the rear sapphire or quartz window, observed experimentally as a dip in the water/window interface velocity using VISAR [Fig. 20(b)]. A sapphire witness is used to record the shot-to-shot variation in the shape of the ramp compression wave and to determine the pressure drive on the front surface of the baseplate[17] needed to simulate the half of the target containing the thin water layer.

Preliminary analysis suggests that the freezing pressure increases from 7 to 9 GPa over compression rates of 0.2 to 2 GPa/ns. Data are being compared to the results of previous experiments on the liquid–ice VII phase transition at 10× lower compression rates and to predictions using *SAMSA*, an LLNL kinetics code.

Development of a Focusing Spectrometer for L-Edge EXAFS
Principal Investigator: F. Coppari
Co-investigators: A. Coleman, A. Krygier, and Y. Ping (LLNL); and L. Gao, K. W. Hill, P. Efthimion, and M. Bitter (Princeton Plasma Physics Laboratory)

EXAFS (extended x-ray absorption fine structure) spectroscopy is a powerful x-ray probe to determine the local structure and disorder of materials at extreme conditions, including those generated by laser-driven compression.[18,19] To collect high-quality EXAFS data, a bright x-ray source and a high spectral resolution spectrometer are needed, especially when studying the material L edge, where the absorption cross section is significantly lower than the K edge. To enable collection of L-edge EXAFS data at the Omega Laser Facility, we developed a new platform for EXAFS measurements based on the use of a Ti-foil backlighter coupled with a focusing spectrometer. Previous backlighter development campaigns demonstrated that Ti foils can generate continuum
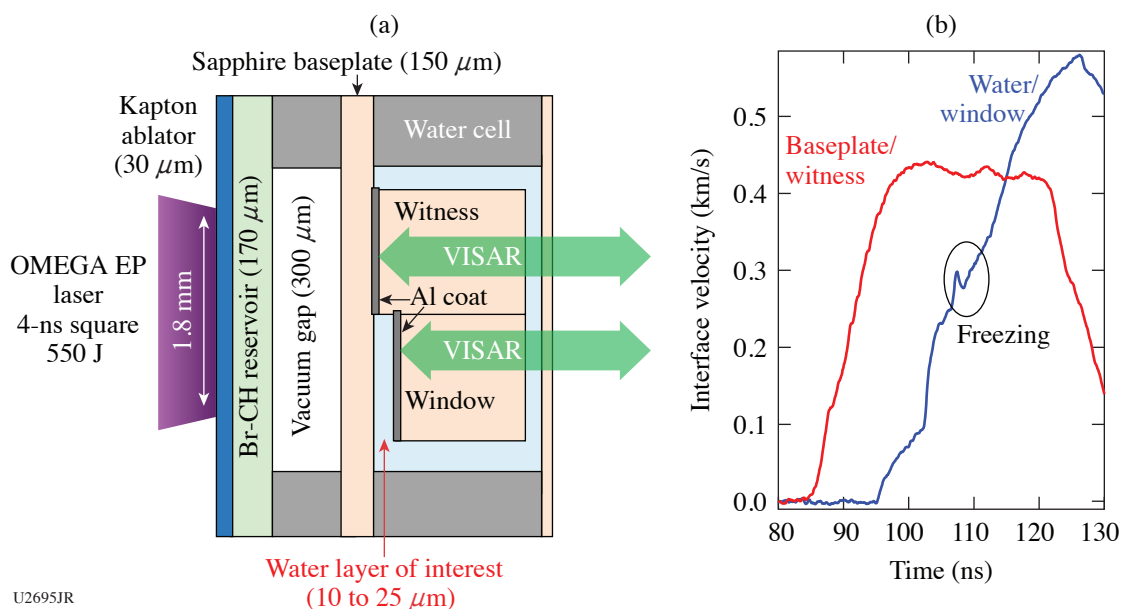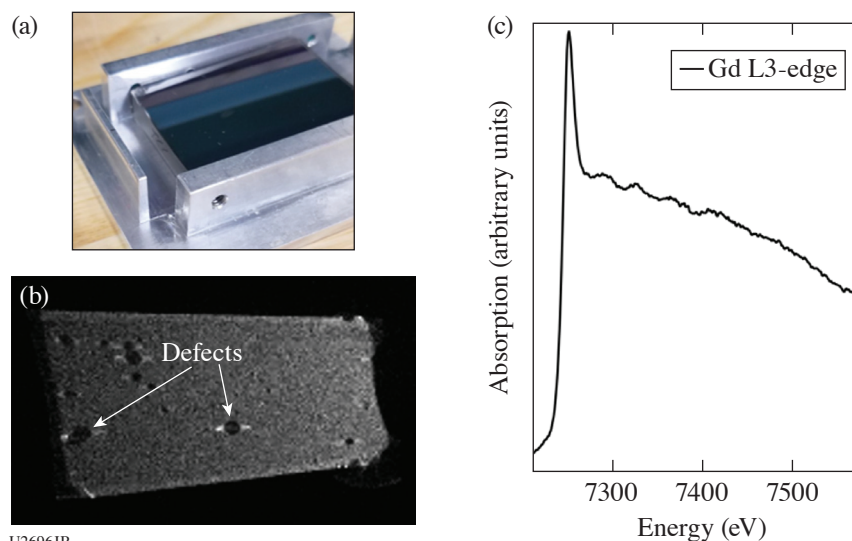
Figure 20

(a) Schematic of water target and (b) velocities of the baseplate/witness interface (red curve) and water/window interface (blue curve) measured using VISAR for shot 31422. The dip in the water/window interface velocity near 110 ns corresponds to freezing in the thin water layer.

emission brighter than capsule implosions[20] especially at x-ray energies >10 keV. The x-ray source size is also bigger ($\sim$300 μm), requiring instruments insensitive to source-size broadening, such as a spectrometer with focusing geometry. The imaging x-ray Thomson spectrometer (IXTS) spectrometer[21] was therefore modified to enable EXAFS measurements around 7 keV. A Ge(220) curved crystal was designed to fit the existing spectrometer body [Fig. 21(a)] and used in two half-days on the OMEGA laser to collect EXAFS data at the Gd L3 edge, for a total of 12 target shots. Preliminary characterization of the performance of the new configuration is necessary, including off-line laboratory tests aimed at verifying the dispersion and focusing geometry, plus dedicated flat-field shots to check potential crystal defects that may interfere with the data [Fig. 21(b)].

Good-quality EXAFS data at the Gd L3 edge were collected [Fig. 21(c)], demonstrating enhanced performance of this new configuration in measuring L-edge EXAFS data with respect to the previous attempts based on capsule implosion and a flat

Figure 21

(a) Photograph of the new Ge(220) crystal used in the IXTS spectrometer to collect EXAFS data. (b) Image of the crystal showing some defects that may interfere with the EXAFS measurement. (c) Absorption spectrum of Gd (L3 edge at 7243 eV) at ambient conditions before flat-field correction. The feature around 7500 eV may be due to a crystal defect.

crystal spectrometer, where a good signal-to-noise ratio was obtained by averaging over multiple shots.[22] This is a key result in support of the ongoing effort of developing the EXAFS platform on the NIF.

EXAFS Measurements of Shock- and Ramp-Compressed Fe Using the IXTS Spectrometer for Temperature Determination

Principal Investigator: A. L. Coleman
Co-investigators: F. Coppari, Y. Ping, and J. McNaney

Temperature determination is one of the greatest challenges in modern laser-driven, dynamic compression experiments. The nanosecond time scales and extreme pressure and temperature conditions at which these experiments are conducted mean that the successful implementation of a temperature diagnostic is challenging and frequently not possible at all. A potential means of obtaining temperature information about a shock- or ramp-compressed sample lies in the analysis of EXAFS data. As a material becomes hotter, thermal motion of the atoms becomes important and reduces the amplitude of the EXAFS oscillations in a manner that is proportional to the temperature increase [Fig. 22(a)].

The purpose of this campaign was to optimize the IXTS[23] spectrometer [Fig. 22(b)] to obtain high-quality EXAFS data from Fe at a series of either shock- or ramp-compressed states, with the intention of determining the sample's temperature through the analysis of the EXAFS spectra. As well as running IXTS as the primary diagnostic, VISAR data were also obtained to establish the pressure in the Fe sample. Over the course of the two half-day campaigns, 12 shots were taken. Shock-compressed, ramp-compressed, and ambient data sets were obtained along with a flat-field shot (taken once every campaign), which are used to correct the effects of the IXTS crystal defects on the EXAFS data. This experimental configuration made use of a Ti foil backlighter x-ray source, driven by a 1-ns laser pulse.[24] While the ramp target package comprised a diamond/Fe/diamond sandwich structure, a tamper layer was implemented in the shock target, consisting of a material that was closely impedance matched to the Fe layer of interest; the purpose of this additional layer was to hold a steady shock pressure state in the Fe layer for the entire 1-ns duration of the backlighter x-ray source.

U2697JR
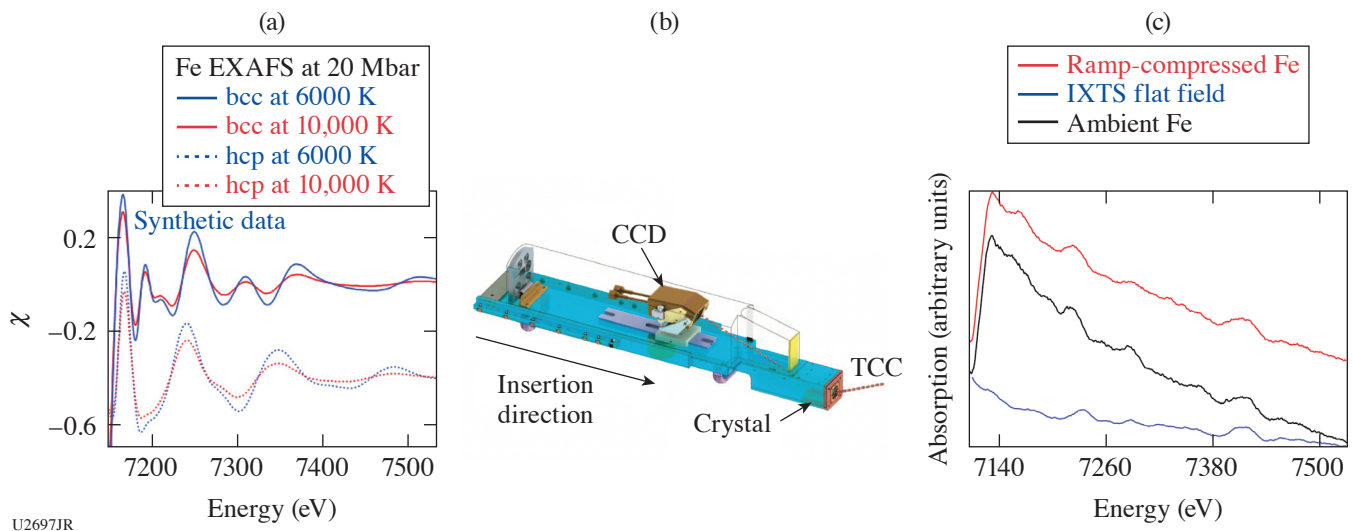
Figure 22

(a) Simulated Fe EXAFS data are shown at various temperatures, exemplifying the reduction in oscillation amplitude due to increased heat. (b) The IXTS spectrometer schematic is shown.[23] A curved Ge(220) crystal is used to observe the energy range around the Fe absorption edge (7.1 keV). (c) Ambient (black curve) and compressed (red curve) absorption spectra of Fe collected during these campaigns are shown along with the flat-field signature of the crystal (blue curve). Bumps in the flat-field data occur as a consequence of crystal defects.

During these campaigns several shielding materials were used to reduce the effect of preheating of the target from the x-ray source. The quality of the data obtained during this experiment was very high, and while the temperature determination analysis

is an ongoing effort, the implementation of this target to access shock- and ramp-compressed states in Fe can be considered to be successful.

Laser-Driven Acceleration of Diamond Flyer Plates

Principal Investigator: F. Coppari

Co-investigators: A. Lazicki, M. Millot, R. London, H. Whitley, and D. Braun

We are developing a platform for performing reference-free equation-of-state measurements of materials in the multi-Mbar regime to be used as an absolutely calibrated pressure standard in future equation-of-state measurements.

We used the OMEGA EP laser to accelerate diamond flyer plates to hypervelocities across a vacuum gap of known thickness and used the VISAR diagnostic to observe the impact of the flyer onto a diamond window (symmetric impact). VISAR provided a measure of the flyer velocity (from which the particle velocity can be obtained) and the shock velocity, before and after the impact, respectively. From these two observables the pressure–density relation of diamond can be obtained by solving the Rankine–Hugoniot equations.[25]

A tailored, ramped pulse shape was used to slowly accelerate the flyer up to peak velocity [Fig. 23(a)], avoiding melting and keeping its density close to ambient density. The impact generates a reflecting shock in the diamond window when the propagated shock is strong enough to melt the window.

Previous data collected at the Omega Laser Facility reached U_s = 24 to 26 km/s. The goal of the OMEGA EP campaign was to take advantage of the higher laser energy to generate stronger shocks and characterize the diamond Hugoniot equation of state above 20 Mbar. Our goal was achieved in five target shots on a day shared with another campaign.

Hydrodynamic simulations were run to optimize pulse shape and target design, and the VISAR data analysis suggests good predictive capabilities. Loss of reflectivity over a couple of nanoseconds was observed [Fig. 23(b)]; the cause is still under investigation. Data analysis will allow us to establish the diamond EOS in an unprecedented pressure range.
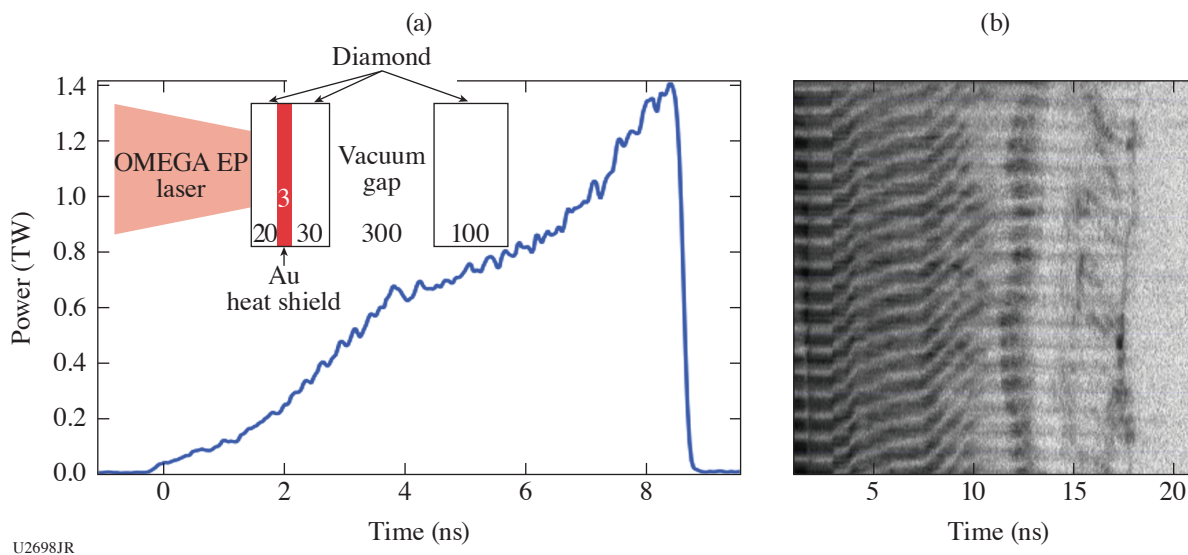
Figure 23
(a) Target design and experimental laser pulse shape. The OMEGA EP laser is focused onto the diamond flyer (consisting of a diamond ablator, Au heat shield, and diamond pusher), separated by a vacuum gap from the diamond window. The laser pulse was specifically designed to slowly accelerate the diamond flyer plate, avoiding shock formation. (b) VISAR data were collected to measure the flyer velocity prior to the impact and the shock velocity in the window after the impact.

Measuring the Effect of Phase-Plate Speckle Imprint on Plastic Ablators Using 2-D VISAR (OHRV)

Principal Investigator: M. Gorman
Co-investigators: R. Smith, S. Ali, and P. M. Celliers

The goals of these experiments were to investigate (1) the laser imprinting from phase-plate speckle onto plastic (CH) ablators and (2) how these instabilities are smoothed, as a function of the CH thickness. The effect of smoothing by spectral dispersion (SSD) on shock roughness was also investigated. At Omega, the 1-D VISAR provides a record of the compression history within the CH sample, and the 2-D VISAR [known as the OMEGA high-resolution velocimeter (OHRV)] provides a high-resolution spatial map of the CH interface velocity and reflectivity at effective single-time "snapshots" during the compression.

As the laser-produced plasma expands, the incident laser radiation gets absorbed up to the critical density (Fig. 24). Absorption of the laser light couples energy into the CH ablator at or below the critical electron density, and electron heat conduction carries some of this energy from the absorption zone to the ablation front. The phase-plate intensity structure becomes smoothed by lateral transport through the plasma and during shock transit within the CH ablator. The target design for shock roughness measurements consists of different thicknesses of polyimide in the 13- to 75-μm range and a LiF [100] window. To enhance reflectivity, the inner surface of the LiF is coated with 0.2 μm of Al. An ~1-μm glue layer is used to adhere the LiF and CH layers. The velocity of the CH/LiF interface is measured by 1-D VISAR and OHRV systems.
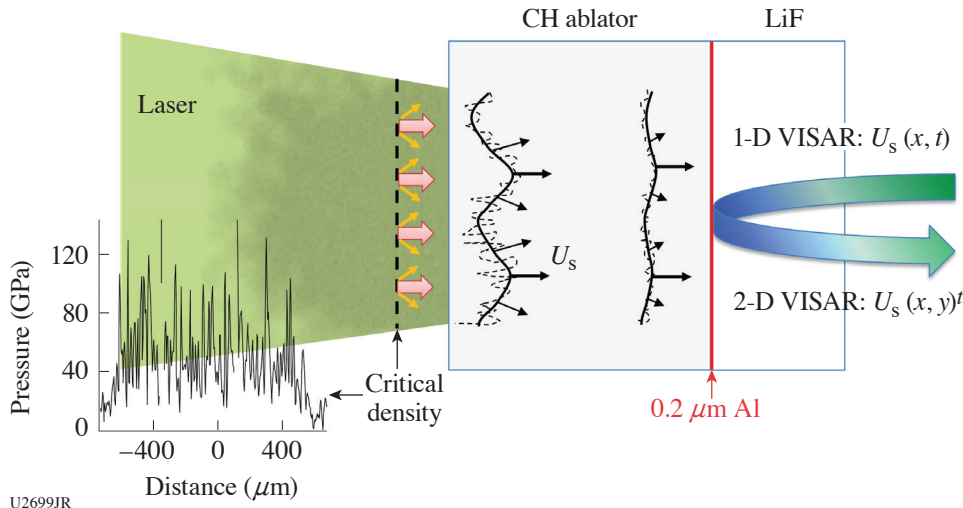

Figure 24
Experimental design. Laser speckle due to phase-plate uniformities impart instabilites in the shock front onto the CH ablator, which are transmitted through to the sample layer. Our experiments use the OHRV system on OMEGA to quantify the shock roughness as a function of CH ablator thickness.

U2699JR

Our results show a clear trend of decreasing shock roughness with CH ablator thickness (Fig. 25). Interestingly, our results also show that the use of SSD is effective in dramatically reducing shock roughness, even in relatively thin CH ablators. These results have important implications for future target designs of laser-driven compression experiments at x-ray free-electron facilities where small-scale laser systems necessitate the need for thinner ablators to reach high sample pressures.

Measurements of Release Isentropes of Proton-Heated Warm Dense Matter with Streaked X-Ray Radiography

Principal Investigators: S. Jiang, Y. Ping, and A. Lazicki
Co-investigators: M. P. Hill (AWE); and A. Saunders, A. Do, D. Swift, J. Nilsen, P. A. Sterne, H. Whitley, and J. H. Eggert (LLNL)

This campaign comprised one day on OMEGA EP during FY20. Following our previous FY19 campaign, which demonstrated the platform to measure the release isentrope of materials heated isochorically using proton heating, the FY20 campaign further used specially designed targets to measure the initial bulk temperature with SOP, and a Thomson parabola along with RCF films to record the spectrum and angular distribution of the proton source.
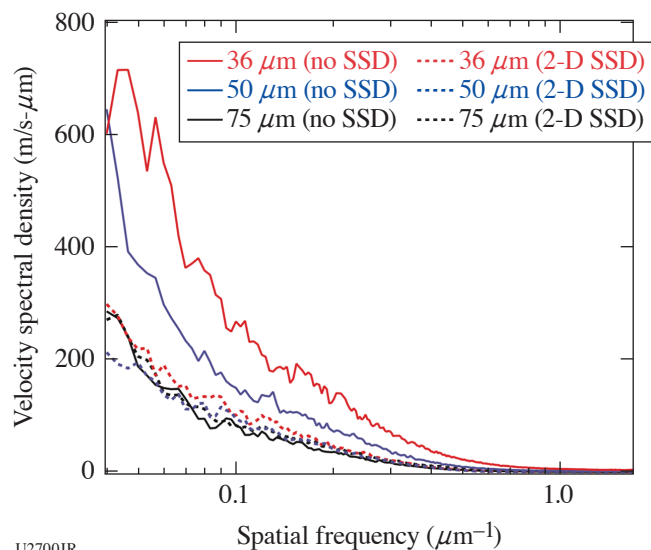
Figure 25
Smoothing of particle velocity map is evident as ablator thickness increases. SSD has little relative effect on the roughness of a 75-μm CH ablator but is found to dramatically reduce the roughness in the thinner ablators.

The experiment used the OMEGA EP short pulse to generate a beam of protons, which heated a 500-μm $\times$ 50-μm $\times$ 50-μm Al ribbon offset from the proton source. Three long-pulse beams were used to heat a V backlighter to provide an x-ray source for streaked x-ray radiography. The time-dependent density profiles calculated from the radiography data were then integrated to obtain pressure–density isentropes [Fig. 26(a)]. The initial bulk temperature was difficult to measure on-shot, however, because the SOP on TIM-12 can be pointed only to the side of the target that was scraped directly by the proton beam. The initial surface temperature on the target side was therefore around 20 to 30 eV—much higher than the bulk temperature. The FY20 campaign used a target that involves a Si mirror on the backside of the 50-μm-thick Al foil. The mirror reflected the emission from the back surface to the SOP, and we were able to derive both the spatial and the temporal temperature distribution of the proton-heated bulk Al. Figure 26(b) shows an initial temperature of around 1.3 eV, which is much lower than the previously measured surface temperature on the side of the Al ribbon.

To account for shot-to-shot variability, the on-shot proton spectrum was also recorded, and we have performed Monte Carlo simulations to calculate the total proton energy deposition inside the target. Preliminary analysis indicates that the energy deposition from an earlier shot shown in Fig. 26(a) is about 3$\times$ higher than that from the shot in Fig. 26(b); therefore, the initial bulk temperature for the isentrope in Fig. 26(a) is estimated to be around 4 to 6eV, which is relatively consistent with model predictions. Further analysis is in progress, and future experiments have been planned over a wider temperature range to benchmark different EOS models.

Measuring Off-Hugoniot Equation of State by Shocking Porous Metals
Principal Investigator: A. Lazicki-Jenei
Co-investigator: S. Jiang, F. Coppari, D. Erskine, R. London, J. Nilsen, and H. Whitley (LLNL); and M. C. Marshall (LLE)

This campaign was designed to use the crushing of pores in an initially porous sample to achieve a hot, solid-density state ahead of the shock front to experimentally access a hotter shock adiabat. Data off of the principal Hugoniot have the potential to provide a more-discriminating test of theoretical models.

The campaign was allocated one half-day and one full day of shots in FY20, for a total of a total of 19 shots (Fig. 27). The first half-day was meant to measure principal and off-Hugoniot states of copper by shocking samples of full-density and ~80% porous material. Targets with diamond ablators and quartz impedance-matching standard were mounted on a halfraum that was driven with 21 beams along the H7–H14 axis; shock velocity and/or transit time in adjacent samples of quartz and porous metal were measured using the VISAR and SOP diagnostics.
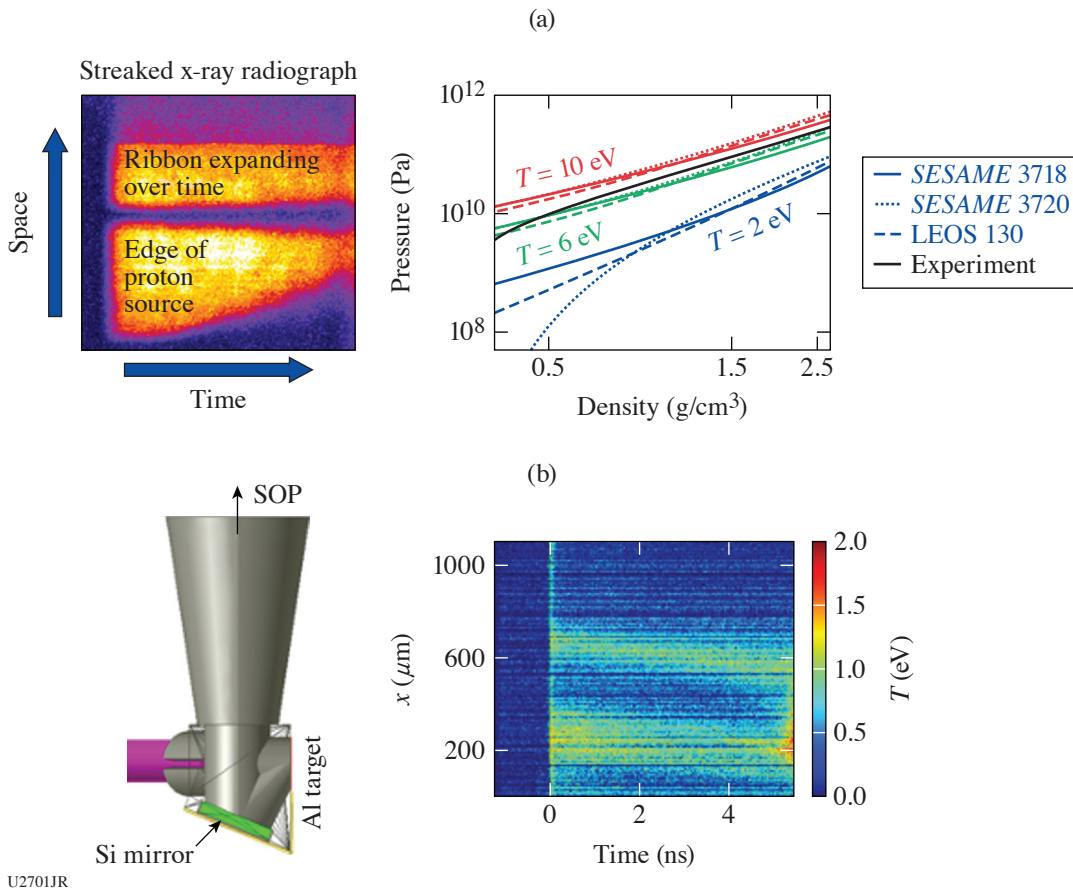
Figure 26
(a) Streaked radiography data and the extracted pressure–density isentrope curve. Isentrope curves from various EOS models at different initial temperatures were also plotted for comparison. (b) Target designed for bulk temperature measurement and SOP data from a 50-μm-thick Al foil.
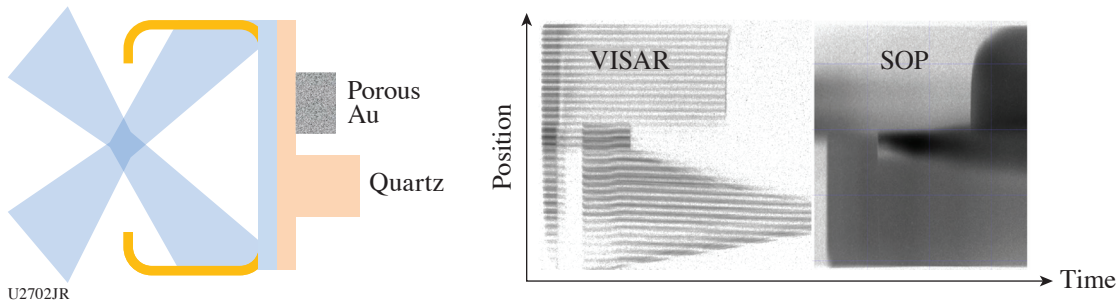
Figure 27
(a) Target configuration with VISAR and SOP data from one shot in the porous EOS-20B Campaign, designed to measure principal- and off-Hugoniot states of Au. (b) The VISAR diagnostic registers the *in-situ* velocity in the quartz impedance-matching standard, and VISAR and SOP record the shock transit time through the Au sample.

    The porous Cu material was made by alloying Cu with Zn and then removing the Zn component, leaving a uniformly distributed network of submicron pores, and giving the material a bulk density of 1.40($\pm$0.05) g/cm^3. The porous samples were very difficult to machine and suffered from high surface roughness and thickness nonuniformity, which was very evident in the VISAR and

SOP data. The sample quality was not adequate for a high-accuracy measurement, but the results were nevertheless important for testing the target and laser drive design. The first half-day was followed by extensive work on target-fabrication methods, and the second full day of shots aimed to measure Hugoniot and off-Hugoniot states of Au. The ~70% porous Au samples were made from an Au–Ag alloy with the Ag removed, and the quality was significantly improved. On the second day we successfully shot four full-density Au samples and seven porous samples, varying the drive energy to span a range of shock pressures. We also shot two samples of Cu to complete work from the first half-day and to test the use of fluorescence spectroscopy to measure temperature information. Previous work with smaller hohlraums had successfully pumped Cu fluorescence using the hohlraum radiation. We did not register a spectroscopic signature on either shot, suggesting that the Cu samples were too thick and the radiation from the hohlraum was likely too low in energy.

3. Material Dynamics, Strength, and Ejecta Physics

Characterizing Laser-Driven Tin Ejecta Microjet Interactions with X-Ray Radiography
Principal Investigator: A. M. Saunders
Co-investigators: C. Stan, S. Ali, K. Mackay, T. Haxhimali, Y. Ping, F. Najjar, B. Morgan, J. H. Eggert, and H.-S. Park (LLNL); and H. G. Rinderknecht (LLE)

The OMEGA and OMEGA EP Ejecta Campaigns seek to develop platforms that investigate ejecta microjet interactions. The microjetting process occurs when a shock wave travels through a sample and interacts with surface defects, such as scratches, dents, or grooves, on the back surface of a sample. The features invert as a limiting case of the Richtmyer–Meshkov instability to form micro-jets.[26,27] Many experiments have been performed to understand the effect of experimental parameters like drive pressure, drive-time dependence, and material type on the jetting process and the resulting jet mass and velocity distributions, but very few examples in the literature seek to understand the effects of microjet interactions.[28,29] To that end, the ejecta campaigns seek to characterize ejecta microjet interactions with x-ray radiography as a way to understand the physical properties governing microjet interaction behavior.

A schematic of the platform can be seen in Fig. 28(a). Two tin foils are situated opposite from each other and are connected to each other by a thin stalk. Each foil has an angular trench carved across the inside of the foil, as seen in Fig. 28(b). The main drive lasers (on OMEGA) or laser (on OMEGA EP) impinge upon the outsides of the tin samples, and ejecta microjets are driven toward each other into the center of the sample as depicted. We then use a point x-ray source in conjunction with an image plate to take
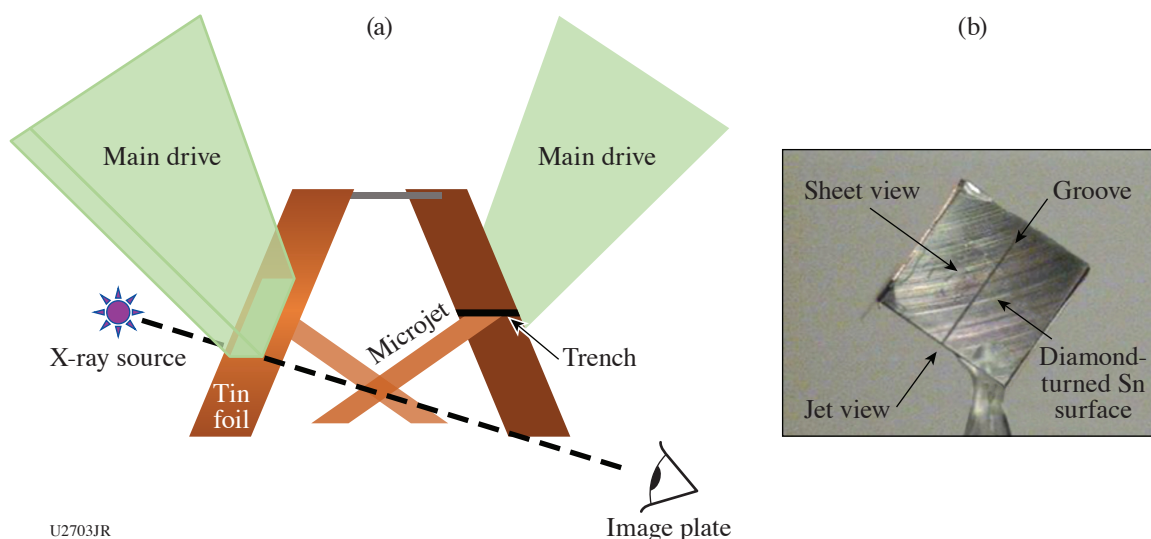
Figure 28
(a) A schematic of the interacting microjet platform and the primary imaging diagnostic. The two tin foils are oriented toward each other, and lasers incident on the back sides of the samples drive ejecta microjets into the center. An x-ray source and image plate serve to take time-resolved radiographs of the system. (b) A photo of the bottom of a piece of tin. The groove is clearly visible carved into the diamond-turned tin surface.

x-ray radiographs of the sample. On OMEGA, the x-ray source consists of a Ti foil offset from a pinhole in order to create a Ti He$_\alpha$ x-ray point source; on OMEGA EP, the x-ray source is a Ti microwire driven by the OMEGA EP short-pulse beam to generate a broadband x-ray source. The primary difference between the OMEGA EP and the OMEGA platforms is the angle at which the microjets interact; due to the nature of the OMEGA laser, the microjets can interact nearly head-on, whereas the OMEGA EP geometry is limited to oblique interactions.

Data from both OMEGA EP and OMEGA platforms show promise with resolving microjet interaction behavior. Figure 29 shows schematics and sample data from both platforms.
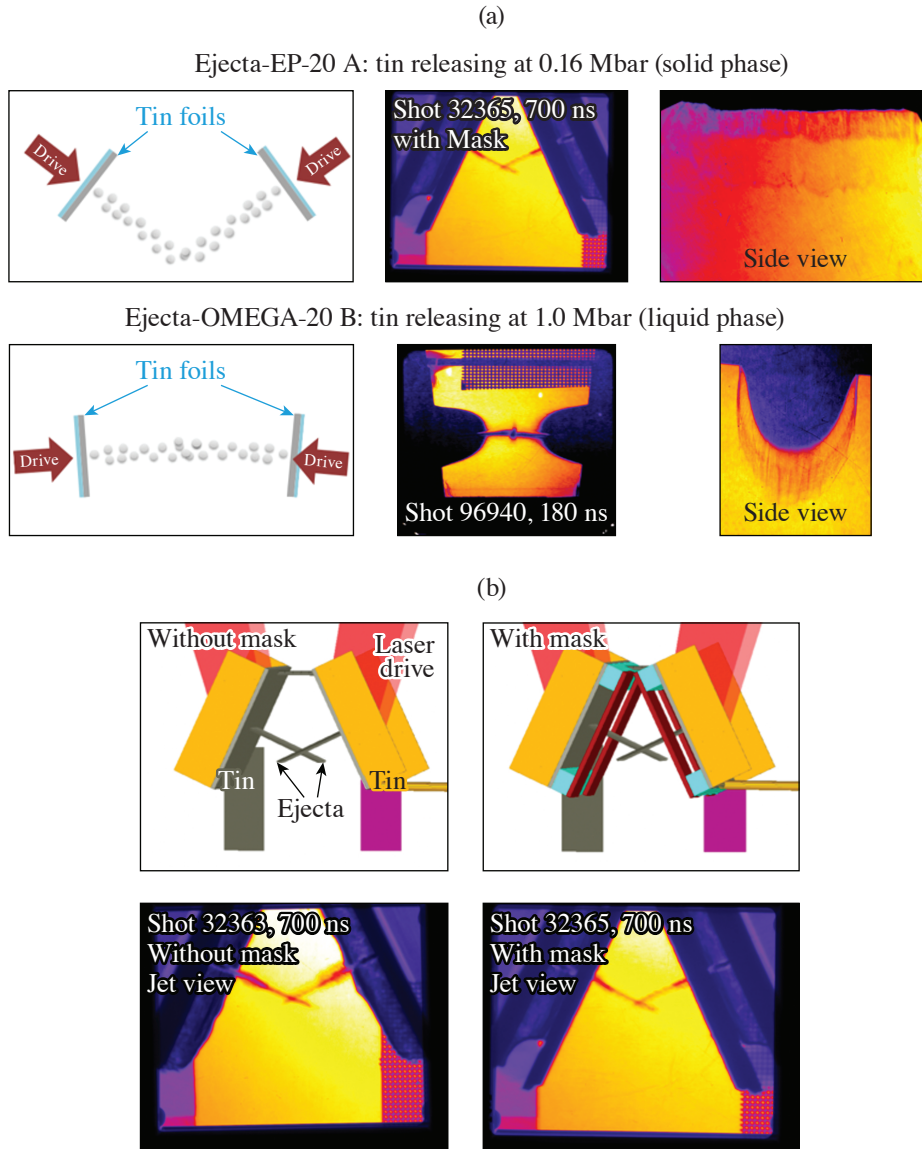
Figure 29

(a) Example data from both the OMEGA and the OMEGA EP platforms. The data on OMEGA EP were taken with a tin release pressure at 0.16 Mbar, which is assumed in the solid phase. The interaction behavior looks markedly different from that observed on the OMEGA platform at 1.0 Mbar, which is believed to be liquid on shock. The side view of the images is shown in both cases, demonstrating the increased planarity with the larger phase plates on OMEGA EP. (b) VisRad models from the OMEGA EP platform showing the addition of masks to reduce the region of microjet that reaches the interaction point. As observed in the data, the masks improve data quality and our ability to resolve absolute density.

Data from both OMEGA EP and OMEGA platforms show promise to resolve microjet interaction behavior. Figure 29(a) shows schematics of the interactions, as well as data looking down the region of interaction for the interacting jets and from the side view for a single jet. We see that the microjets from tin releasing into solid at 0.16 Mbar appear to pass through each other unaffected, while the microjets from tin releasing into liquid at 1.0 Mbar form a cloud at the interaction point. More studies remain to be done to determine if the difference in interaction behavior is due to the difference in densities of the microjets or from other materials properties.

Figure 29(b) compares radiographs of the nominal target design taken at the same time after the laser drive was turned on versus a target with the addition of Ta masks on the bottom side. The Ta masks restrict the region of microjetting material that is able to reach the center and allows for better resolution of jet characteristics and interaction behavior. The masks are one such improvement that has been implemented over the course of these campaigns.

Overall, the radiographs show great promise in their ability to study microjet interactions. Further work involves measuring interactions at more drive pressures and on different materials, as well as performing quantitative analyses on the x-ray spectrum so that we can measure the density of microjetting material to a high accuracy. The results will allow for refinement of models used in laboratory hydrocodes that have been described in several publications.[30,31]

Understanding the Strength of Diamond Under Shock Compression
Principal Investigator: C. Stan
Co-investigators: H.-S. Park, C. Wehrenberg, and A. Krygier (LLNL); and M. Hill (AWE)

Diamond, or HDC, is a critical material for ultrahigh dynamic-compression experiments, in both materials strength and ICF. It possesses extremely high hardness, thermal conductivity, and optical transparency and is therefore used as either a window or capsule material across a wide variety of experiments. Its behavior above the Hugoniot elastic limit is poorly understood. Recent diffraction work shows that it may retain strength up to 20 GPa when compressed to 150 to 300 GPa (Ref. 32). Here, we shock-compress diamond and measure velocimetry and Laue diffraction. Two backlighter types were used: a capsule and a Ge foil.

Both backlighter types show elongated single-crystal diffraction spots (Fig. 30). These are indicative of a single crystal under longitudinal deformation, where deformation is occurring on the unit cell level. In the Ge backlighter shots, the diffraction patterns are stronger, and powder diffraction from the pinhole and an Au powder layer can also be seen. These lines should aid in positional calibration of the image plates during diffraction analysis. Overall, the Ge backlighter provided better experimental data.
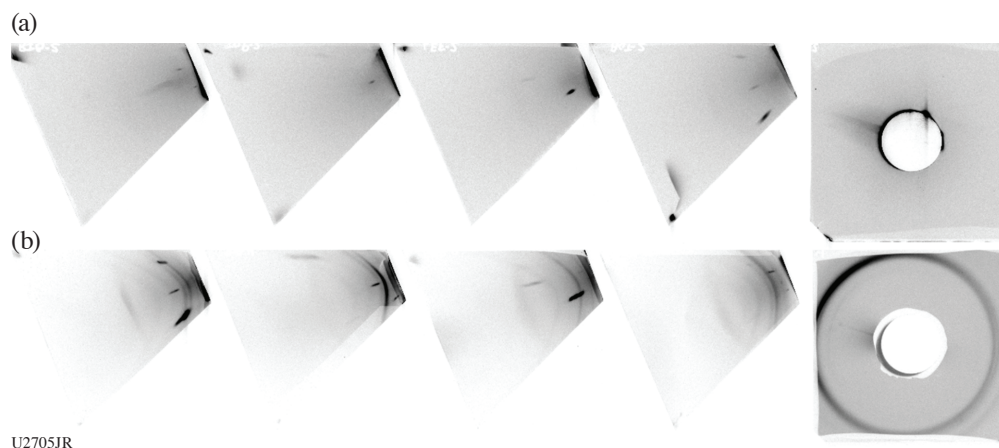

Figure 30
(a) Image plates from a capsule backlighter shot; (b) image plates from a Ge backlighter shot.

Measuring Tin Strength Using the Rayleigh–Taylor Instability

Principal Investigators: C. Stan, H.-S. Park, T. Lockard, and D. Swift (LLNL): M. Hill (AWE); G. Righi (University of California, San Diego); and D N. Polsin (LLE)

We measure plastic deformation in tin using directly driven targets with seeded sinusoidal perturbations. The targets consist of a Be ablator (20 μm), a brominated plastic layer (20 μm), epoxy (5 to 7 μm), rippled tin (40 μm), a LiF window (500 μm), and fiducials. Radiography data were collected at varying points in time (20 to 50 ns from laser start time) to determine ripple growth [Fig. 31(a)]. Growth factor was determined from the images using two different methods. In the first method, which we refer to as direct amplitude analysis,

$$\mathrm{GF} = \frac{A_{\mathrm{driven}}}{A_{\mathrm{undriven}}}, \tag{1}$$

where GF is the growth factor and A is the amplitude of the driven and undriven ripples in units of photostimulated luminescence (PSL). In the second method, the modulation transfer function (MTF) method,

$$\mathrm{GF} = \frac{\rho \Delta z_{\mathrm{driven}}}{\rho \Delta z_{\mathrm{undriven}} \, \mathrm{MTF}}, \tag{2}$$

where $\rho \Delta z$ is the areal density determined from fiducial wedge steps and MTF is determined from a Fourier transform across the knife edge. The MTF provides a measure of the x-ray beam spot size for the measurement and therefore determines the instrumental resolution.

Initial analysis using the MTF analysis method [Fig. 31(b)] shows that the growth was lower than anticipated by Steinberg–Guinan strength modeling.[33]

U2706JR
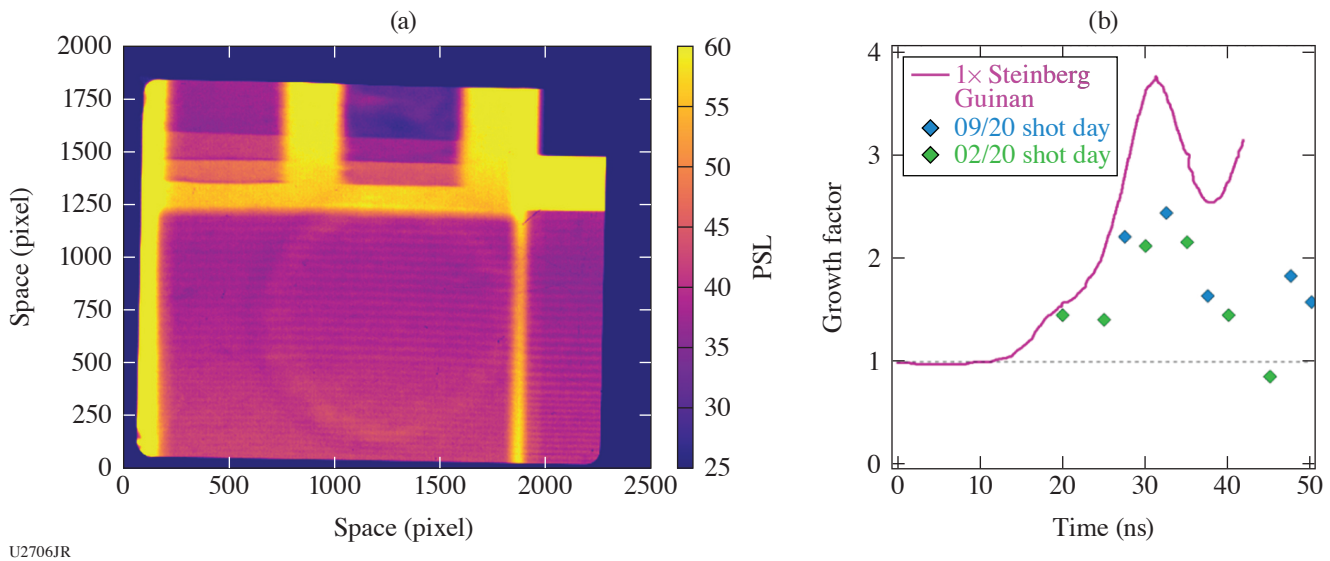
Figure 31
(a) Typical radiography image, collected at 37.5 ns after the laser is turned off. Fiducial steps and a gold knife edge can be seen at the top of the image; to the right are fiducial rippled steps. The imprint of the directly driven laser can be seen in the center. (b) Growth factor derived from ripple amplitude analysis using the gold knife edge and fiducial steps; values for the two shot days are represented, as well as growth predicted by the Steinberg–Guinan model.[33]

4. National Security Applications

Enhancement via Magnetic Fields of Bremsstrahlung X-Ray Source

Principal Investigator: P. L. Poole

Co-investigators: S. C. Wilks, M. May, K. Widmann, and B. E. Blue

High-fluence x-ray sources can be used for extreme radiation environment effects testing,[34] including nuclear survivability. Facilities like the NIF and Z can readily produce high fluences of x rays under 10 to 20 keV, but high-photon energy versions of those line-emission–dominated sources are considerably weaker. The SRS-XRay Campaign on OMEGA investigates a different x-ray–generation mechanism that produces a bremsstrahlung spectrum using the hot electrons accelerated from strong plasma waves within the target.

In this campaign, two MIFEDS coils[35] were utilized to generate an axial magnetic field within gold hohlraums of two different sizes and with a variety of foam and parylene (CH) fills. Here the fields act to constrain plasma flow, prolonging the duration of high plasma density and temperature that is beneficial to plasma-wave formation. Two such coils were fielded, allowing a maximum of 30-T field to be present within the target plasma. Figure 32 shows the x-ray output for >70-keV photons measured with (blue curve) and without (orange curve) the B field present.

The observed enhancement via B field is in agreement with simulations and will provide information for an upcoming NIF shot campaign.
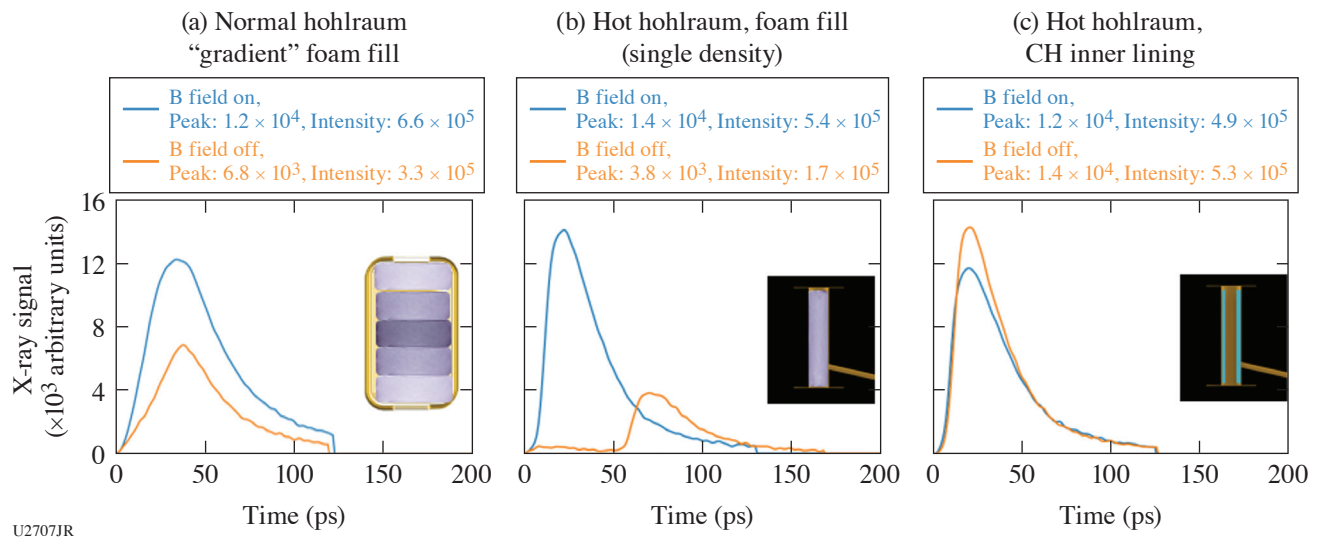

(a) Normal hohlraum "gradient" foam fill
B field on, Peak: 1.2×10^4, Intensity: 6.6×10^5
B field off, Peak: 6.8×10^3, Intensity: 3.3×10^5

(b) Hot hohlraum, foam fill (single density)
B field on, Peak: 1.4×10^4, Intensity: 5.4×10^5
B field off, Peak: 3.8×10^3, Intensity: 1.7×10^5

(c) Hot hohlraum, CH inner lining
B field on, Peak: 1.2×10^4, Intensity: 4.9×10^5
B field off, Peak: 1.4×10^4, Intensity: 5.3×10^5

U2707JR

Figure 32

X-ray signal from channel 3 ($\geq$70-keV photons) for three different target types (shown in insets). Blue curves are with the B field on; orange curves are with B field off. A 2$\times$ to 3.5$\times$ increase in peak x-ray signal in this range is observed for the two foam-filled hohlraum types.

The Effect of Target Geometry on Multi-keV Line Emission from Nanowire Cu Foams

Principal Investigator: M. J. May

Co-investigators: G. E. Kemp, R. Benjamin, J. D. Colvin, T. Fears, F. Qian, and B. Blue

High-intensity x-ray sources in the 1- to 30-keV spectral range, needed for various HED and ICF applications, have been under development for the past 20 years. The direct irradiation of a material at solid densities has poor coupling of the laser energy into heating the material and creating a plasma. The x-ray emission has been found to be the most efficient in targets where the created plasma is underdense to laser light, with the electron density $n_e < 0.25\ n_c$. In underdense plasmas, the heat front can propagate supersonically through the target, which allows full volumetric heating of the emitting material by the laser. A large fraction

of the target material can be ionized to the appropriate charge state to produce an efficient x-ray source. Freestanding metallic nanowire foams[36] have been found to be a promising candidate that can be used to produce intense x-ray emission.[37] Nanowire foams of Cu, Ag, and Au have been successfully fabricated into targets having average densities of 6 to 20 mg/cm^3, which makes the created plasma underdense to laser light by design. The question arises whether we can affect the x-ray emission by changing the target geometry. Since these targets tend to expand hydrodynamically, constraining the expanding plasma inside a thin plastic tube could increase the yield. The x-ray emission could be reduced, however, from thermal conduction losses to the tube wall.

The experimental configuration is shown in Fig. 33(a). Cu nanowire foams at ~10 mg/cm^3 [Fig. 33(b)] were irradiated with 20 kJ of laser energy in a 1-ns pulse with IDI-300 phase plates to produce ~8-keV K-shell line radiation. A total of six shots were executed, with half of the targets being freestanding Cu nanofoams. The other half of the targets were mounted in plastic tubes with a wall thickness of 50 μm. These cylindrical targets were 2 mm in diameter and 2 mm in length. All the lasers were pointed at the ends of the targets.

The K-shell x rays were recorded with Dante (0 to 20 keV), the Henway x-ray spectrometer (6 to 13 keV), and the LLNL multipurpose spectrometer (MSPEC). The target x-ray emission was imaged using the soft x-ray (SXR) imaging snouts to understand the evolution of the different emission patterns from the two types of targets. Initial results suggest that encasing the nanowire foam inside a tube enhances the emission by ~20% when compared with emission from the freestanding nanowire foam. Figure 33(c) compares voltage versus time of the Cu-filtered channel from Dante. Clearly the plastic-encased target shows ~20% enhancement in the x-ray emission. The spectra from the Henway spectrometer also show a similar increase. Detailed simulations are needed to better understand this effect.
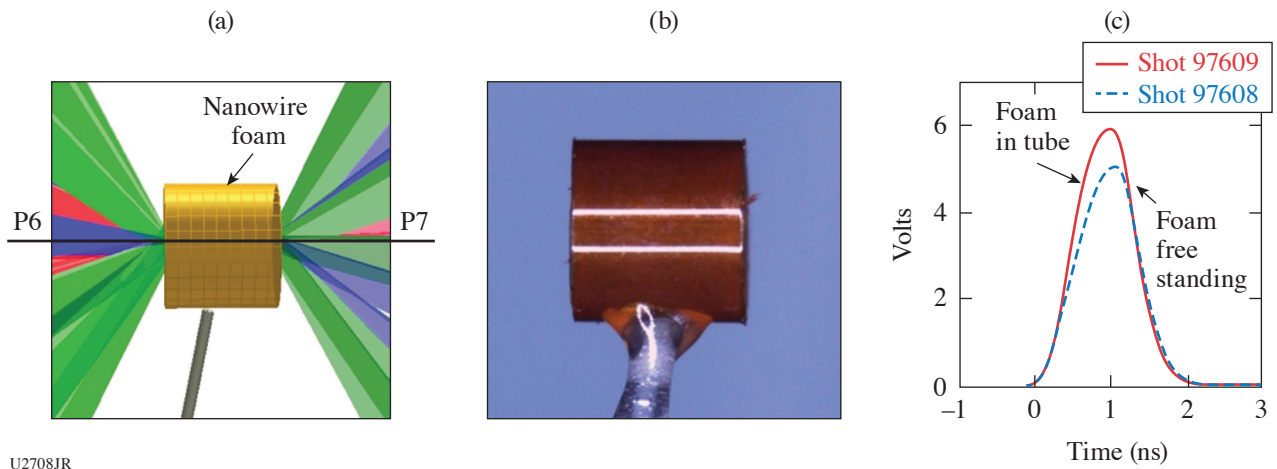

Figure 33
(a) Experimental configuration for NanoFoam-20A. (b) Image of a Cu nanowire foam target in a plastic tube. (c) Comparison of the voltages of a Cu-filter Dante channel measured from a freestanding and a tube-encased Cu nanowire foam target.

Enhancing Multi-keV Line Radiation from Laser-Driven Plasmas Through the Application of External Magnetic Fields
Principal Investigator: G. E. Kemp
Co-investigators: D. A. Mariscal, P. L. Poole, J. D. Colvin, M. J. May, and B. E. Blue (LLNL); C. K. Li and A. Birkel, (MIT); E. Dutra (Nevada National Security Site); and J. L. Peebles, D. H. Barnak, and J. R. Davies (LLE)

A recent LLNL LDRD effort (17-ERD-027) that studied the influence of externally applied magnetic fields on laser-driven x-ray sources—like those typically used for high-fluence radiography or backlighters—focused on improving multi-keV characteristic x-ray emission conversion efficiency through thermal transport inhibition. The MagXRSA-20A Campaign was the third and final iteration of a platform demonstration series exploring the potential risks and benefits of applying externally generated B fields to previously fielded x-ray sources on the OMEGA laser. This recent campaign pushed to maximize the B-field strength

to 40 T (versus 20 T from MagXRSA-19A), into a regime where little to no data currently exist for such high-Z, non-LTE (local thermodynamic equilibrium), magnetized plasma conditions. The data from this platform will be used to constrain thermal transport inhibition and MHD models currently used in the multi-physics radiation-hydrodynamic code *HYDRA*.[38]

The experimental configuration is illustrated in Fig. 34(a). Thin-walled, cylindrical Kr gas pipes (1.5 atm) were irradiated with 20 kJ of laser energy in a 1-ns pulse—a typical source of ~13-keV K-shell line radiation. A total of six shots were taken, half of which had externally imposed B fields. A dual-MIFEDS design was adopted to reach ~40-T axial B-field strengths. The primary goal of the shots was quantifying changes in x-ray emission with increasing external B-field strength, recorded with Dante (0 to 20 keV), hard x-ray detectors (20 to 500 keV), pinhole cameras [>2 keV, Fig. 34(b)], and the dual-channel spectrometer (11 to 45 keV). Secondary diagnostics included stimulated Raman/Brillouin laser backscatter and proton radiography using a D^3He backlighter capsule as a source of 3- and 15-MeV protons. Analysis is ongoing, but initial results suggest ~1.5× enhancements in >8-keV Kr K-shell emission and ~3.3× improvement in >80-keV continuum emission with a 40-T field; the enhancement effect appears to saturate at around 20 to 30 T, which is consistent with pre-shot modeling.[39]

The successful demonstration of this platform has motivated the development of a magnetized x-ray source platform on NIF—dubbed MAGNETO—where ~1.5 to 2× improvements in Ag K-shell (~23-keV) emission from nanowire foam sources have already been observed with a 25-T field (shot N200609-002) provided by the new MAGNIF pulser.[40]
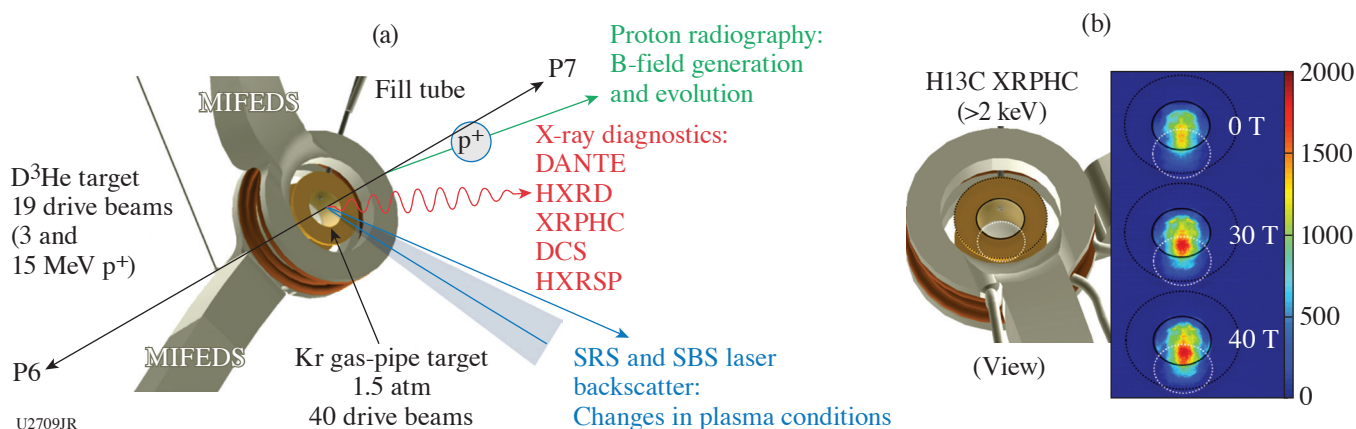

Figure 34
(a) Experimental configuration for MagXRSA-20A. X-ray emission, laser backscatter, and proton radiography data were simultaneously obtained to quantify the influence of external B fields on laser-driven Kr plasmas. (b) Representative time-integrated x-ray pinhole data illustrating the saturation of the B-field effect; roughly 30% higher >2-keV integrated signals were observed for fields 20 T and above.

Improving Exploding-Pusher Performance with Optimized Pulse Shapes
Principal Investigator: M. Hohenberger
Co-investigators: T. J. B. Collins and M. J. Rosenberg (LLE); and L. Divol, C. Yeamans, B. E. Blue, and W. W. Hsing (LLNL)

Experiments were conducted to study the performance of exploding-pusher (XP) target implosions using computationally optimized pulse shapes to maximize the neutron yield. The yield from XP's primarily stems from shock heating of the fusionable fill gas, and these implosions exhibit low convergence, low areal densities, and high ion temperatures. XP's are typically driven by single shock pulse shapes, e.g., Gaussian, flattop, or ramped pulses, and, by virtue of their shock-driven nature, are insensitive to degradation mechanisms that affect high-convergence implosions, such as electron preheat or Rayleigh–Taylor instabilities. While neither yield amplification nor a propagating burn is accessible at these conditions, significant neutron yields in excess of 10^{16} have been demonstrated on the NIF, making XP's a robust source for, e.g., nuclear effects studies and other applications.

Glow-discharge plasma (GDP) targets with an 860-μm outer diameter and 8-μm-thick walls and filled with 10 atm of room-temperature D_2 gas were symmetrically imploded using all 60 OMEGA beams with ~250 J/beam. As shown in Figs. 35(a)–35(c) as
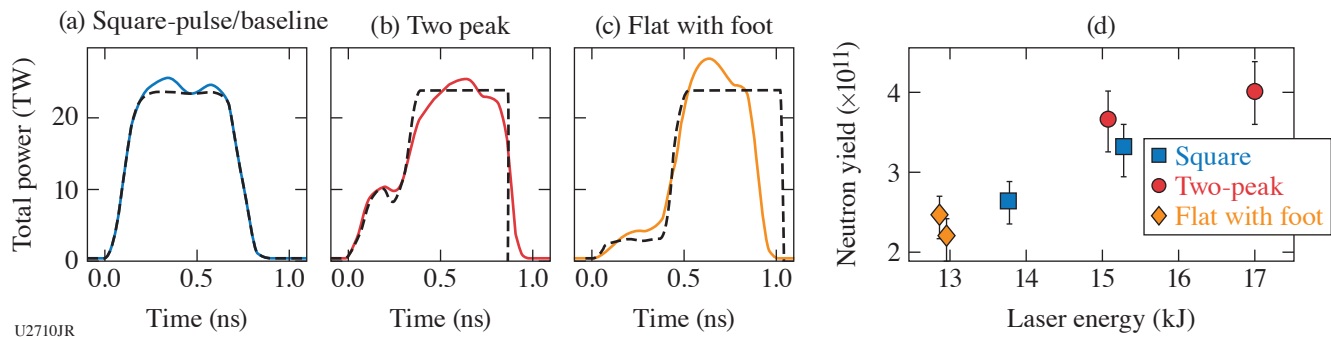
Figure 35

Exploding-pusher performance was tested with three pulse shape designs: (a) square pulse as a reference, (b) a two-peak design, and (c) a flattop with foot. Experimental pulse shapes (solid lines) suffered from pulse-shaping difficulties, and both shaped pulses in (b) and (c) underperformed in energy compared to the requests (dashed lines). (d) Experimental neutron yields scaled with incident laser energy, but differences between requested and delivered pulse shapes make a correlation between performance and pulse shape difficult.

dashed lines, three different pulse shapes were compared: a simple flattop as a baseline reference [Fig. 35(a)] and two multi-shock pulse shapes based on computational optimization using the hydrodynamic code *Telios*,[41] which in simulations improved both the free-fall and total yield by >40% compared to the baseline. The experimental pulse shapes [dashed lines in Figs. 35(a)–35(c)] qualitatively reproduced the optimized pulses, but difficulties in the pulse shaping resulted in reduced energy by as much as 25%.

Experimental yields are shown in Fig. 35(d) for the three designs as a function of total laser energy. Notably, while the yield appears to roughly scale with incident energy, an assessment of performance with respect to pulse shape is difficult given the differences in total energy and shock timing compared to the optimized requests. Post-shot simulations are currently in progress, but preliminary results indicate that (1) the experimental performance trends are captured well by simulations[42] and (2) that experimental yield increase of the order of 30% beyond the baseline may be feasible with improved pulse shaping of the multi-shock designs.

5. Plasma Properties

Measurement of Au M-Shell Emission Using a Buried-Layer Platform
Principal Investigator: E. V. Marley
Co-investigators: R. F. Heeter, M. B. Schneider, G. E. Kemp, M. E. Foord, D. A. Liedahl, and J. Emig (LLNL); and D. Bishel (LLE)

This campaign was designed to measure emitted M-shell gold spectra from a well-characterized and uniform plasma to benchmark atomic kinetic models. The buried-layer target geometry used for this experiment is capable of generating plasmas with an electron temperature of ~2 keV at electron densities of 10^{21} electrons per cubic centimeter. Similar plasmas have also been found inside gold hohlraums during ICF experiments on the NIF. The OMEGA laser–target configuration provides a stable platform to create uniform plasmas for radiation transport and atomic kinetic studies at relevant conditions.

Planar, buried-layer targets were illuminated equally on both sides (Fig. 36) to heat the sample. The sample used in the campaign was a 1300-Å-thick Au/V mixture (0.27/0.73 by atoms) designed to burn through completely before the end of the laser pulse, resulting in highly uniform plasma conditions to measure the M-shell emission of the gold. The samples were buried between two 5-μm-thick layers of Be, which acted as an inertial tamp, slowing the expansion of the sample. This campaign was a repeat of the FY19 campaign, correcting for a target-fabrication issue, which had previously compromised the hydrodynamic behavior of the expanding plasma.

Time-resolved 2-D images of the target's x-ray emission, viewed both face on and side on, were recorded using pinhole cameras coupled to framing cameras. The 4ω probe beam and Thomson spectrometer were also used to measure scattering, including both
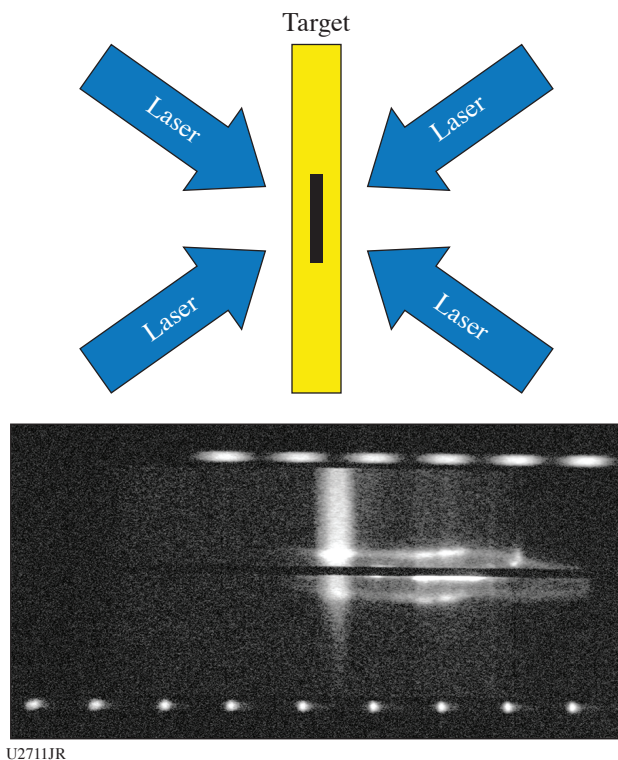
Figure 36
Experimental configuration and Thomson-scattering data of shot 96710.

U2711JR

the electron and ion-acoustic features (see Fig. 36). A new optical filter package was used during the campaign to filter out the self-emission and unconverted light, which has been an issue in the past with high-Z targets, and good-quality data were obtained. The K-shell spectra from the V were used to determine the electron temperature of the plasma. The time-resolved spectra were recorded using a crystal spectrometer coupled to a framing camera. Two crystal spectrometers were used to record the full range of the Au M-shell emission, also time resolved. All of the framing cameras, those used for imaging as well as those used for spectroscopy, were co-timed so the plasma conditions could be determined for the measured Au M-shell emission.

A single pulse shape was used during the campaign, a 3.0-ns square pulse with a 100-ps picket arriving 1 ns before the main pulse. A complete set of data from all six diagnostics, fully cross-timed, was recorded during the campaign at temperatures ~2 keV.
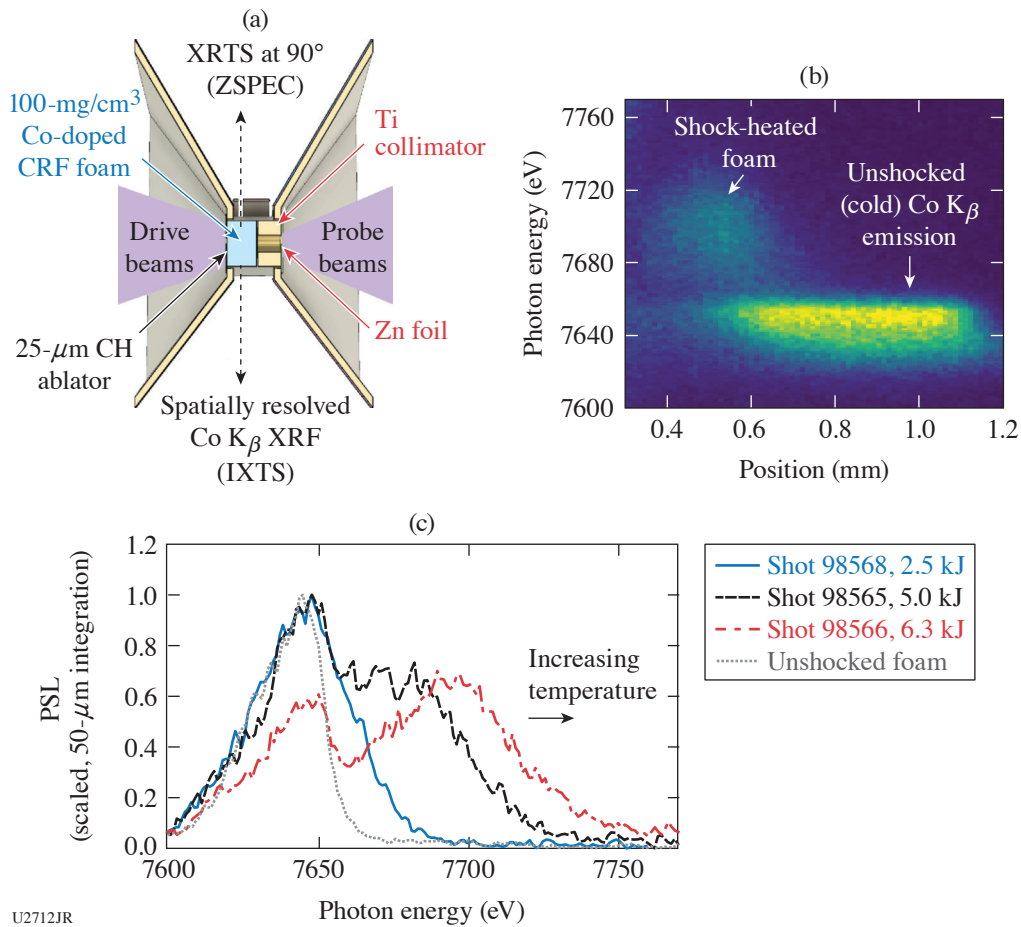
Developing a Robust Temperature Diagnostic for High-Energy-Density Experiments Using X-Ray Fluorescence Spectroscopy
Principal Investigator: M. J. MacDonald
Co-investigators: T. Döppner, A. M. Saunders, H. A. Scott, and T. Baumann, (LLNL); S. R. Klein, M. P. Springstead, H. J. LeFevre, K. Ma, C. C. Kuranz, and E. Johnsen (University of Michigan); and R. W. Falcone (University of California, Berkeley)

Although temperature is a fundamental parameter in plasma physics, a limited number of experimental diagnostics exist to measure temperature in HED experiments. In particular, measurements of temperatures relevant to HED hydrodynamic experiments (tens of eV) are typically limited to surface measurements or very low densities where absorption spectroscopy can be used with soft x rays. The FoamXRFTS Campaign aims to develop x-ray fluorescence (XRF) spectroscopy as an *in-situ* diagnostic for temperatures as low as 10 eV using K-shell fluorescence of mid-Z elements in combination with time-resolved x-ray Thomson scattering (XRTS).

In these experiments, planar shocks were driven into Co-doped carbon foams and probed using a Zn He$_\alpha$ x-ray source as shown in Fig. 37(a). The Zn He$_\alpha$ probe both excites Co K-shell XRF and serves as the source for the XRTS measurements to independently measure the plasma temperature. An example of the XRF data collected using the IXTS is shown in Fig. 37(b), where the spatially resolved measurement separates emission from the shock-heated foam and the unshocked foam. The change

(a)

XRTS at 90°
(ZSPEC)

100-mg/cm^3
Co-doped
CRF foam

Ti
collimator

Drive
beams

Probe
beams

Zn foil

25-μm CH
ablator

Spatially resolved
Co K$_\beta$ XRF
(IXTS)

(b)

Shock-heated
foam

Unshocked
(cold) Co K$_\beta$
emission

(c)

Increasing
temperature

— Shot 98568, 2.5 kJ
--- Shot 98565, 5.0 kJ
-·- Shot 98566, 6.3 kJ
······ Unshocked foam

U2712JR

Figure 37

(a) Target geometry showing the foam driven from the left, the Zn probe on the right, and the x-ray spectrometers viewing perpendicular to the shock direction. (b) Example of spatially resolved Co K$_\beta$ XRF emission measured using the IXTS showing the increased Co K$_\beta$ emission energy from the shock-heated foam and the cold emission from the upstream, unshocked foam at ambient conditions. (c) Comparison of three shots from the FoamXRFTS-20B Campaign at three drive energies, resulting in different Co K$_\beta$ emission energies that can be used to infer temperature.

in the Co K$_\beta$ emission energy is caused by the increased ionization state of the Co at higher temperatures. Figure 37(c) compares three drive energies from the FoamXRFTS-20B shot day, clearly demonstrating the sensitivity of the Co K$_\beta$ energy to the drive conditions. The XRF data collected using this platform will be extremely valuable in designing HED experiments using XRF as an *in-situ* temperature diagnostic.

Obtaining high-quality XRTS spectra using this platform has been an ongoing challenge, with background-scattering sources obscuring the scattering data. An updated target design used on the FoamXRFTS-20B shot day significantly improved the quality of the XRTS data and is currently being analyzed.

6. Hydrodynamics

Microwire to Wire Preheat is Primarily Due to Soft X Rays
Principal Investigators: S. F. Khan, D. Martinez, S. Wilks, and D. H. Kalantar (LLNL); and D. Mastrosimone and D. Haberberger (LLE)

Previous OMEGA EP experiments demonstrated preheat occurring between high-energy microwire backlighter systems when the time delay between the short-pulse laser illumination of the wires was longer than 5 ns (for wires 5 mm apart). The 4ω

probe shadowgraphs (Fig. 38) of one of the tungsten wires show a material expansion of ~5× after 15 ns, resulting from local absorption of the other wire's emission.

In the FY20 DoubleHEBL (high-energy backlighter) experiments, we concluded that the hot electrons emitted from the first wire are not a substantial contributor to the preheat experienced by the other wire by using an ~8-T magnetic field (generated by MIFEDS) to divert electrons (<5 MeV) from impacting the second wire. We took a shot with the B field off, and both shots show the same amount of wire preheat, indicating that the primary mechanism of preheat is not affected by a magnetic field. In a separate configuration, we used a 25-μm-thick polyimide shielding between the two microwires, which successfully prevented preheat expansion. Using transmission attenuation tables, x rays less than 1.5 keV are ~99% blocked by this shielding. In addition to the 4ω probe shadowgraphy data, the relative wire sizes in these experiments were tracked by inferring the resolution (Fig. 39) from the potentially preheated wires by radiographing a solid tungsten-carbide sphere. Simulations are in progress to better understand the mechanisms involved in microwire preheat.
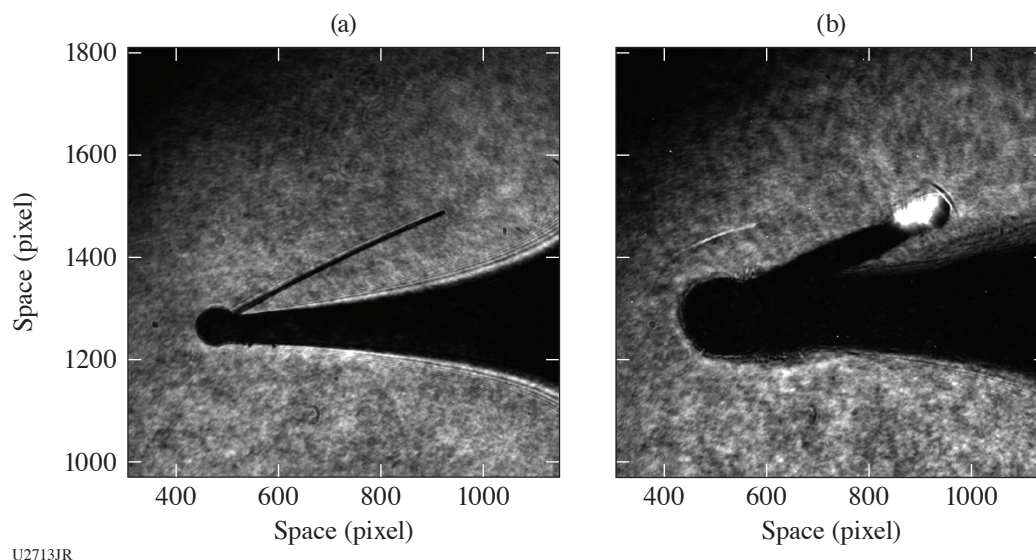

U2713JR

Figure 38
The 4ω probe shadowgraphs of a 12.5-μm tungsten wire (a) before and (b) after being exposed for 15 ns to the radiation from another nominally identical wire. Both the wire holder and the wire show an expanded size after the exposure. The bright spot in the left image is the emission when the short pulse hits the wire *after* the 4ω probe laser pulse. Images from shot numbers 33296 and 33297 (10 September 2020).
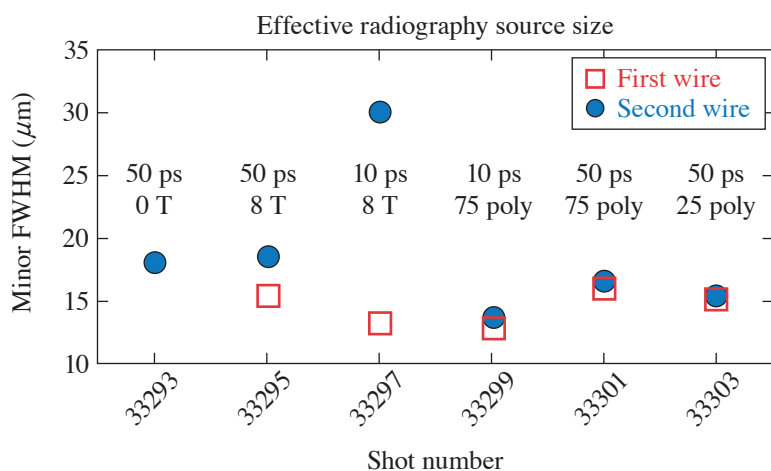

U2714JR

Figure 39
Plot of the inferred source size (resolution) from the microwires. The 50 ps/10 ps indicate the laser pulse duration (with 1 kJ/0.9 kJ). The higher-intensity short pulse clearly generates more preheat expansion (shot 33297 versus 33295). In addition, there is an indication of self-generated preheat (shot 33299 versus 33301) where both wires have a better resolution with the shorter pulse. Shot 33293 versus 33295 shows the same expansion with and without B field. Finally, comparing shot 33297 to 33299 shows the benefit of the polyimide for shielding the second wire.

Wakefield X-Ray Source for Radiography Above 100 keV

Principal Investigator: F. Albert

Co-investigators: M. King (LLNL and University of Texas, Austin); N. Lemos, J. Williams, and H. Chen (LLNL); J. L. Shaw and D. H. Froula (LLE); and M. Sainclair and C. Joshi (University of California, Los Angeles)

X-ray backlighting is one of the most commonly used methods to look into the extreme temperatures, pressures, and densities created during laser-driven HED science experiments. Over the years, much effort has gone into developing backlighting techniques to look into these states of matter with new sources and diagnostics. The properties of an x-ray backlighter (flux, source size, spectrum, duration) required for an experiment depend on the application being studied and the quantity being measured. The goal of the Wakefield-EP shot series is to develop a new type of x-ray backlighter, which could be advantageous for applications requiring broadband spectra, small source sizes (sub-50 μm), short duration (less than 10 ps), and x rays extending beyond 100 keV. Our proposed x-ray sources are based on laser wakefield acceleration (LWFA) of electrons in the self-modulated regime (SMLWFA). Specifically, we aim to develop three different x-ray sources based on betatron radiation, Compton scattering, and bremsstrahlung emission.

The Wakefield-EP-20A shot day aimed at producing and detecting betatron radiation produced by SMLWFA using a modified version of the EPPS diagnostic. We enlarged apertures to 5 mm (instead of 1 mm) and included a hole at the back of the magnet box, as well as a stack of nine image plates at the back of the TIM boat to detect betatron radiation. Initial analysis of our experiments shows that EPPS was successful at simultaneously recording electron, spectrum, profile, and x-ray data.

The wakefield platform produced robust electron beam data, recording a >100-nC charge electron beam at each shot, as well as two-temperature spectra extending up to about 200 MeV. The signal-to-noise ratio must be further improved for more-efficient x-ray detection. Monte Carlo simulations are providing additional diagnostic shielding enhancements for the next shot day in February 2021.

Supersonic-to-Subsonic Transition of Radiation Transport in Silica Aerogel

Principal Investigators: D. Rusby, F. Albert, R. A. Colón Quiñones, C. Harris, S. Murray, S. Prisbrey, and H. K. Widmann (LLNL); and H. G. Rinderknecht (LLE)

In laser-driven ramp-compression experiments aimed at measuring the equation of state of various materials, an incident shock can reflect at the interface between low and high impedance layers and the reflected shock subsequently interacts with the incident shock. Within this context, it is critical to understand how well radiation-hydrodynamic codes capture the physics of colliding shocks or pressure fronts. The ESPADA platform was designed for this purpose. ESPADA-20A, the first campaign on OMEGA, observed the shock front induced by the supersonic-to-subsonic transition of a Marshak wave in silica aerogel and compared the results with the radiation-hydrodynamic code *KULL*. Supersonic-to-subsonic radiation transition induces a diagnosable shock wave that can be observed with x-ray radiography.

During this initial half-day of shots, a halfraum was driven to temperatures ~120 eV by 21 OMEGA beams (3-ns flattop pulse with 273 J/beam). This x-ray drive launched a Marshak wave through a 2-mm-diam, 2-mm-long, 30-μm-thick gold tube filled with SiO_2 foam (33 mg/cm^3) attached on the other side of the halfraum. A 12-μm-thick Ti foil was driven with 21 additional beams to provide a near-monochromatic 4.7-keV x-ray backlighter source oriented quasi-perpendicular to the gold tube's axis. A 200-μm-wide slit on each side of the tube allowed the x rays to pass through the foam, and the x-ray images of the target were recorded on a four-strip x-ray framing camera at different times (Fig. 40).

Our initial results (Fig. 40) show reasonable agreement between the experiment and simulations.[43] The larger discrepancy observed at early times is possibly due to a smaller contrast ratio—a consequence of the lower number of photons of the backlighter in the region corresponding to earlier times. For our next experiment in January 2021 we expect closer comparison with an improved backlighter source, and we will image shock/shock interactions by launching a strong shock (few Mbar) by direct laser ablation from the other side of the target.

(a)

Experimental radiographs (4.7 keV)

4.6 ns

5.1 ns

Induced shock

5.6 ns

U2715JR

(b)

4.6 ns (experiment)
4.6 ns (simulation)
5.1 ns (experiment)
5.1 ns (simulation)
5.6 ns (experiment)
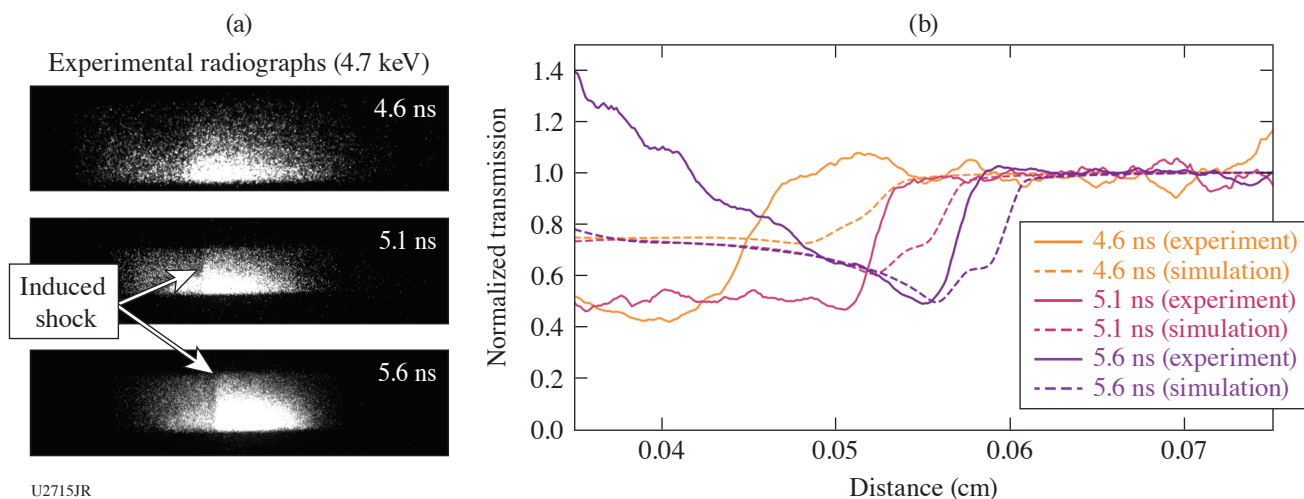5.6 ns (simulation)

Normalized transmission

Distance (cm)

Figure 40
Experimental data with (a) images for the induced shock recorded with x-ray radiography and (b) comparison between experimental and simulated shock location (using the code *KULL*) for different timings.

REFERENCES

1. *LLE 1999 Annual Report*, October 1998–September 1999, 222, Rochester, NY, LLE Document No. DOE/SF/19460-332 (2000).

2. J. H. Eggert *et al.*, Nat. Phys. **6**, 40 (2010).

3. M. Millot *et al.*, Phys. Plasmas **27**, 102711 (2020).

4. S. Le Pape *et al.*, Phys. Rev. Lett. **120**, 245003 (2018).

5. M. Millot *et al.*, Phys. Rev. B **97**, 144108 (2018).

6. M. Millot *et al.*, Nature **569**, 251 (2019).

7. D. K. Bradley *et al.*, Phys. Plasmas **16**, 042703 (2009).

8. D. K. Bradley *et al.*, Phys. Rev. Lett. **102**, 075503 (2009).

9. S. W. Haan *et al.*, Phys. Plasmas **18**, 051001 (2011).

10. J. P. Knauer *et al.*, Phys. Plasmas **17**, 056318 (2010).

11. C. Goyon *et al.*, Phys. Rev. E **95**, 033208 (2017).

12. H. Morita *et al.*, Phys. Rev. E **103**, 033201 (2021).

13. S. Jiang *et al.*, Phys. Rev. Lett. **116**, 085002 (2016).

14. C. Courtois *et al.*, Phys. Plasmas **18**, 023101 (2011).

15. A. G. MacPhee *et al.*, Optica **7**, 129 (2020).

16. M. C. Marshall *et al.*, J. Appl. Phys. **127**, 185901 (2020)

17. D. M. Sterbentz *et al.*, J. Appl. Phys. **128**, 195903 (2020).

18. B. Yaakobi *et al.*, Phys. Rev. Lett. **95**, 075501 (2005).

19. Y. Ping *et al.*, Phys. Rev. Lett. **111**, 065501 (2013).

20. A. Do *et al.*, Rev. Sci. Instrum. **91**, 086101 (2020).

21. E. J. Gamboa *et al.*, Rev. Sci. Instrum. **83**, 10E108 (2012).

22. Y. Ping *et al.*, Rev. Sci. Instrum. **84**, 123105 (2013).

23. E. J. Gamboa *et al.*, Rev. Sci. Instrum. **83**, 10E108 (2012).

24. A. Do *et al.*, Rev. Sci. Instrum. **91**, 086101 (2020).

25. Ya. B. Zel'dovich and Yu. P. Raizer, *Physics of Shock Waves and High-Temperature Hydrodynamic Phenomena*, edited by W. D. Hayes and R. F. Probstein (Dover, Mineola, NY, 2002).

26. R. D. Richtmyer, Commun. Pure. Appl. Math. **13**, 297 (1960).

27. E. E. Meshkov, Izv. Akad. Nauk SSSR, Mekh. Zhidk. Gaza **334**, 151 (1969).

28. W. T. Buttler *et al.*, J. Fluid Mech. **703**, 60 (2012).

29. T. de Rességuier *et al.*, J. Appl. Phys. **124**, 065106 (2018).

30. A. M. Saunders *et al.*, AIP Conf. Proc. **2272**, 120025 (2020).

31. K. K. Mackay *et al.*, J. Appl. Phys. **128**, 215904 (2020).

32. M. J. MacDonald *et al.*, Appl. Phys. Lett. **116**, 234104 (2020).

33. D. J. Steinberg, S. G. Cochran, and M. W. Guinan, J. Appl. Phys. **51**, 1498 (1980).

34. M. J. May *et al.*, Phys. Plasmas **25**, 056302 (2018).

35. O. V. Gotchev *et al.*, Rev. Sci. Instrum. **80**, 043504 (2009).

36. F. Qian *et al.*, Nano Lett. **17**, 7171 (2017).

37. M. J. May *et al.*, Phys. Plasmas **25**, 056302 (2018).

38. M. M. Marinak *et al.*, Phys. Plasmas **8**, 2275 (2001).

39. G. E. Kemp *et al.*, Phys. Plasmas **23**, 101204 (2016).

40. B. Pollock *et al.*, Bull. Am. Phys. Soc. **64**, TO6.00007 (2019).

41. J. A. Delettrez, T. J. B. Collins, and C. Ye, Phys. Plasmas **26**, 062705 (2019).

42. T. J. B. Collins *et al.*, "Optimized Pulse Shapes for Improved Exploding-Pusher Peformance," presented at the 62nd Annual Meeting of the American Physical Society Division of Plasmas Physics, Memphis, TN, 9–13 November 2020.

43. R. Colon Quinones *et al.*, "Shock Wave Formation Induced by the Supersonic-to-Subsonic Transition of Radiation Transport in Silica Aerogel," presented at the 62nd Annual Meeting of the American Physical Society Division of Plasmas Physics, Memphis, TN, 9–13 November 2020.